Time dependent magnetization and stiffness measurements in thin superconducting rings

Bornovski Matan

Time dependent magnetization and stiffness measurements in thin superconducting rings

Research Thesis

Submitted in partial fulfillment of the requirements
for the degree of Master of Science in Physics

Bornovski Matan

Submitted to the Senate
of the Technion — Israel Institute of Technology
Tevet 5786 Haifa December 2025

The thesis was done in the Faculty of Physics under the supervision of Prof. Keren Amit. The author of this thesis states that the research, including the collection, processing and presentation of data, addressing and comparing to previous research, etc., was done entirely in an honest way, as expected from scientific research that is conducted according to the ethical standards of the academic world. Also, reporting the research and its results in this thesis was done in an honest and complete manner, according to the same standards.

Acknowledgments

I'd like to thank Dr. Tomoki Kobayashi and Prof. Atsutaka Maeda from the university of Tokyo for the preparations of the FeSeTe samples.

The Technion's funding of this research is hereby acknowledged.

Contents

List of Figures

Abstract

Superconducting stiffness (ρ_s) and coherence length (ξ) are commonly determined from the penetration depth (λ) and the upper critical field (H_{c2}), respectively. However, determining these parameters in high temperature superconductors, and iron based superconductor in particular, remains challenging. In iron-based superconductors, such as the iron-chalcogenides family, internal magnetic fields can substantially deviate from the applied field due to exchange fields, leading to inaccurate estimates of both quantities. Furthermore, a recent study on bulk single crystals of $FeSe_{0.5}Te_{0.5}$ revealed a "knee" in the temperature dependence of the superconducting stiffness, raising questions about it's origin. To address this problem in $Fe_{1+y}Se_xTe_{1-x}$ ($x = 0.5$, $y \approx 0$), we employed the Stiffnessometer technique on pulsed-laser deposition (PLD) grown thin films of thickness d=80 (nm). the use of thin films offers a more stable stoichiometric homogeneity compared to bulk crystals, yeilding cleaner samples that allow us to disentangle the effects of inhomogeneity and geometry. In this method, a rotor-free vector potential (A) is applied to a superconducting ring, and the resulting current density (j) is extracted from its magnetic moment (m). Using London's relation $j = \rho_s A$ and the Ginzburg-Landau framework, we directly determine both ρ_s and ξ by numerically solving the GL equations for an annular geometry. Our stiffness measurements reproduced the "knee" feature in the the temperature dependence of the the normalized stiffness and using BCS theory reveal the presence of two superconducting gaps ($\Delta_S = 1.06meV$, $\Delta_L = 2.04meV$), with temperature dependence deviating from the conventional BCS two-gap s-wave pairing model. Additionally we calculated the lower critical field, (H_{c1}), and attempt an independent verification using standard magnetization measurements under an applied magnetic field using both field cool (FC) and zero-field cool (ZFC) protocols. In $FeSe_{0.5}Te_{0.5}$ we observe unexpected time-dependent magnetization, with nonlinear dependence as function of ln(t) and switching between negative and positive magnetic moments. These temporal effect prevent the application of conventional flux creep theories. To isolate the source of these temporal effects, we performed similar measurements on a $Nb_{0.61}Sn_{0.27}N_{0.11}$ annulus of comparable geometry (d=80 (nm)). The reproduction of the time dependent behavior supports a geometric origin intrinsic to thin superconducting rings.

Chapter 1

Introduction

Conventional superconductivity, as described by the Bardeen–Cooper–Schrieffer (BCS) theory, involves a phonon-mediated bound state of a pair of electrons (Cooper pair) [1], while it describes some families of superconductors, it fails to capture the behavior of high-temperature superconductors, specifically a relatively new addition to this family, the so called Iron based superconductors, including the relatively new iron-based family and in particular, the promising $FeSe_{0.5}Te_{0.5}$ candidate, which may offer insights into strongly correlated superconductors [2, 3, 4].
In a recent study by Peri et al. (2023) [5], measurements on several bulk $FeSe_{0.5}Te_{0.5}$ single crystal rings revealed a knee feature in the stiffness vs. temperature - a sudden change in slope at a specific temperature. Interestingly, DC magnetization measurements of the rings did not reveal the knee feature. The authors proposed several possible origins for this anomaly:

1. Electronic nematic phase transition.

2. Surface superconductivity - allowing for different critical temperatures for the bulk and surface supercurrents.

3. Multiple Fermi surfaces - accounting for distinct gap formations as function of temperature in different bands.

4. Sample geometry.

However, further investigations were hindered by limitations of the ring geometry and possible stoichiometric inhomogeneities. The origin of the knee feature - whether intrinsic to the material or due to experimental limitations - remained a gap in our current understanding of its properties. To address this, we examined thin film $FeSe_{0.5}Te_{0.5}$ samples, grown using the PLD (Pulsed-Laser Deposition) method, characterized through DC magnetization and Stiffnessometer measurements. Thin films offer multiple advantages:

1. Reduced sample inhomogeneity (whether in rations of Se and Te or excess Fe), resulting in a cleaner platform to probe magnetic responses compared to crystals grown using the modified Bridgman method.

2. Better control over sample geometry.

By measuring the magnetic response as a function of temperature in these films, we aim to determine whether the knee phenomenon is inherent to the material or a byproduct of manufacturing techniques or sample geometry.

This approach allows testing the hypotheses raised by Peri et al. [5], namely: whether the knee originates from nematic order, surface superconductivity, multiple Fermi surfaces, or sample geometry.

Working with thin films requires new analysis methods to extract the stiffness and coherence length [6]. These are described in the main text, and the superconducting properties are presented in great detail.

The knee effect was reproduced in our thin film samples, and from the normalized stiffness we conclude that it originates from multiple Fermi surfaces, as proposed by Peri et al. To check our stiffness measurements we wanted to determine Hc1 and xi (see Eq. 19 at Peri). However, while characterizing our thin samples we noticed an unusual effect, namely, time-dependent and positive magnetization under field-cool (FC) conditions. In zero-field-cool (ZFC) conditions, the time dependence shows a strongly non-linear magnetic response as function of $ln(t)$, an effect that we did not encounter in the literature. Additionally, a switch between positive and negative values in the magnetic moment was observed.

1.1 Superconductivity

Superconductivity is a phase of matter characterized by the Meissner effect (the diamagnetic expulsion of magnetic fields) accompanied by zero electrical resistance below a critical temperature T_c. Two main theoretical frameworks describe this phase: the microscopic Bardeen–Cooper–Schrieffer (BCS) theory and the phenomenological Ginzburg–Landau (GL) theory. Superconductors are classified into two main types according to their thermodynamic and magnetic properties [1]:

- Type I superconductors exhibit perfect diamagnetism for external magnetic fields lower than the thermodynamic critical field H_c, above which superconductivity is completely destroyed.

- Type II exhibit perfect diamagnetism for external magnetic fields lower than the lower critical field, H_{c1}, as the magnetic field increases beyond H_{c1}, quantized magnetic flux lines (vortices) penetrate the superconductor, forming a mixed state in which superconductivity coexists with normal state regions. When the field reaches the upper critical field, H_{c2}, superconductivity is fully suppressed.

1.1.1 London equation

The London equation describes the supercurrent density's response to the vector potential and the superconducting phase [1]:

$$\vec{J_s} = -\rho_s \left(\vec{A}_{tot} - \frac{\Phi_0}{2\pi} \vec{\nabla} \phi \right), \tag{1.1}$$

where $\vec{J_s}$ is the supercurrent density, ρ_s is the superconducting stiffness, $\vec{A_{tot}}$ is the total magnetic vector potential, Φ_0 is the superconducting flux quantum, and ϕ is the phase of the order parameter. The order parameter Ψ is a complex scalar field [1]

$$\Psi\left(\vec{r}\right) = \left|\Psi\left(\vec{r}\right)\right| e^{i\phi(\vec{r})}, \tag{1.2}$$

which vanishes above T_c and, within the Ginzburg-Landau (GL) framework, is proportional to the density of superconducting charge carriers for temperatures lower than T_c.

The stiffness, ρ_s characterizes the rigidity of the superconducting condensate against phase twists of ϕ and is related to the order-parameter modulus and the London penetration depth by [1]:

$$\rho_s = \frac{\left|\Psi\right|^2 e^{*2}}{m^*} = \frac{1}{\mu_0 \lambda_L^2}, \tag{1.3}$$

where e^* is the charge of the superconducting carrier, m^* is the mass of the superconducting carrier, μ_0 is vacuum permeability, and λ_L is the London penetration depth.

1.1.2 Ginzburg-Landau (GL) equations

The GL framework introduces the complex order parameter Ψ and two characteristic length scales: the London penetration depth λ_L and the coherence length ξ. The London penetration depth λ_L is the characteristic length scale for the exponential decay of magnetic field inside a superconductor, and is related to the superconducting stiffness by Equation 1.3. The coherence length ξ is the characteristic scale over which the order parameter varies significantly.

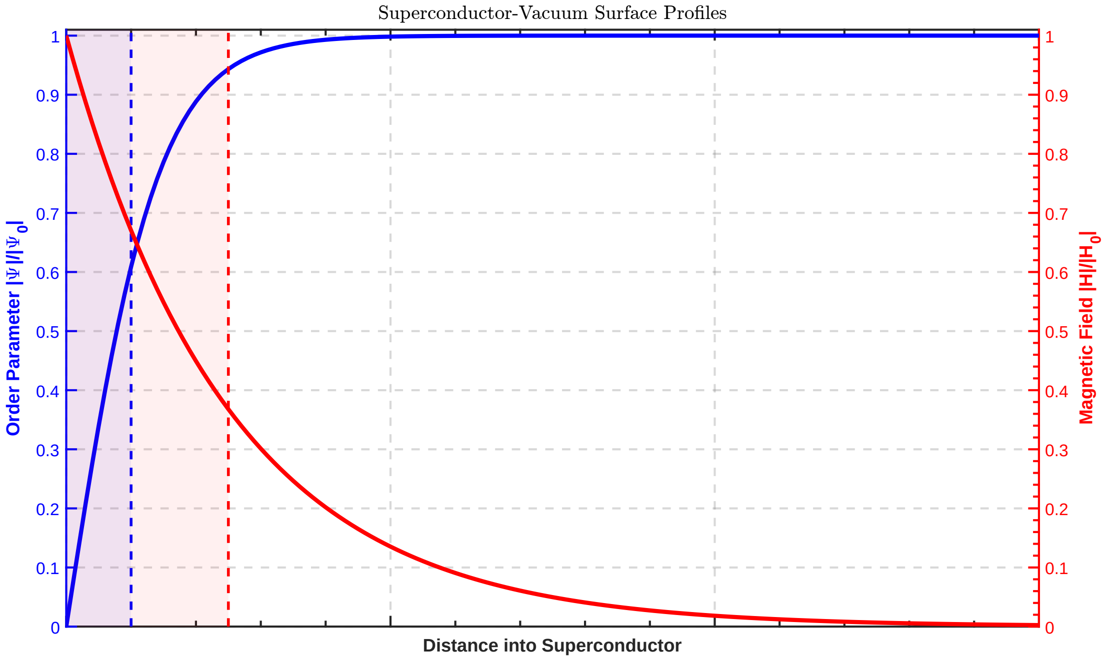

Figure 1.1: Interface between vacuum (left to the graph) and superconductor (plotted region), with profiles of the normalized order parameter (blue) and normalized magnetic field (red). The vertical dashed blue line represents ξ, while the vertical dashed red line represents λ. Adapted from [1].

Figure 1.1 illustrates the interface between vacuum (left) and a superconductor (right). The figure presents the spatial profiles of the normalized order parameter (blue curve) and the normalized magnetic field (red curve) across the superconducting region. The superconducting order parameter rises from zero at the surface to its bulk value (sometimes refereed to as ψ_∞) over a characteristic length scale denoted by the coherence length ξ, marked by the vertical dashed blue line. In a similar way, the magnetic field decays exponentially to zero inside the superconductor over the penetration depth λ, indicated by the vertical dashed red line.

The ratio $\kappa = \frac{\lambda}{\xi}$ determines the superconductor type: type-I superconductors satisfy $\kappa < \frac{1}{\sqrt{2}}$ and type-II satisfy $\kappa > \frac{1}{\sqrt{2}}$ (see Figure 1.1).

From thermodynamical considerations, for non-interacting vortices the line energy at penetration of the vortex is related to H_{c1} by:

$$H_{c1} = \frac{\epsilon_1}{\Phi_0} \tag{1.4}$$

Where ϵ_1 is the vortex line energy per unit length and Φ_0 is the superconducting flux quantum. Equating this to the line energy (field plus kinetic contributions) gives:

$$\epsilon_1 \approx \frac{\Phi_0^2}{4\pi\mu_0\lambda^2}\ln\kappa \tag{1.5}$$

We can then relate, H_{c1} to κ (using the measured λ and ξ) [1, 7]:

$$\mu_0 H_{c1} = \frac{\Phi_0}{4\pi\lambda^2}\ln\left(\frac{\lambda}{\xi}\right). \tag{1.6}$$

GL theory introduces the free energy functional:

$$\mathcal{F} = \int \left[f_{n0} + \alpha\left|\Psi\right|^2 + \frac{\beta}{2}\left|\Psi\right|^4 + \frac{1}{2m^*}\left|\left(-i\hbar\nabla - e^*\vec{A}\right)\Psi\right|^2 + \frac{\left|\vec{B}\right|^2}{2\mu_0}\right] d^n x \tag{1.7}$$

Minimizing this functional yields the GL [1], which describe the superconductor's thermodynamic and electrodynamic properties:

$$\alpha\Psi + \beta\left|\Psi\right|^2\Psi + \frac{1}{2m^*}\left(\frac{\hbar}{i}\vec{\nabla} - e^*\vec{A}\right)^2\Psi = 0, \tag{1.8}$$

$$\vec{J} = \frac{e^*\hbar}{2m^* i}\left(\Psi^\dagger\vec{\nabla}\Psi - \Psi\vec{\nabla}\Psi^\dagger\right) - \frac{e^{*2}}{m^*}\left|\Psi\right|^2\vec{A}, \tag{1.9}$$

where α and β are phenomenological temperature dependent coefficients, and $\hbar$ is the reduced Plank constant. For a spatially uniform order parameter, the second equation reduces to 1.1.

1.1.3 BCS theory

Unlike the phenomenological GL theory, BCS offers a microscopic description of superconductivity. Its key constituents are Cooper pairs - bound states of two electrons created mediated by electron-phonon interaction. These pairs behave as composite bosons and can condense into a coherent macroscopic state.

When the temperature drops below T_c, an energy gap Δ opens at the fermi surface. This superconducting gap represents the finite energy required to break a Cooper pair. In the conventional case, the cooper pairs form a spin singlet state with s-wave orbital symmetry (opposite momenta and spins), corresponding to an isotropic gap function in momentum space. Alternatively,in *d*-wave pairing the gap vanishes along nodal lines in momentum space, leading to a $\vec{k}$-dependent gap $\Delta(T, \vec{k})$.

In the GL framework, Δ is related to the modulus of the order parameter $|\Psi(\vec{r})|$.

In BCS theory, the electrodynamic response of the supercurrent to the vector potential can be expressed in the general form [1]:

$$\vec{J}(T, q) = -K(T, q)\vec{a}(q), \tag{1.10}$$

where q is the Fourier wave-vector, K is the response function, and $a(q)$ is the Fourier component of the magnetic vector potential.

For the DC limit $q \to 0$, this becomes [1]

$$K(T,0) = \lambda_L^{-2}(T) = \lambda_L^{-2}(0)\left[1 + 2\int_{\Delta}^{\infty} \partial_E f \cdot \frac{E}{\sqrt{E^2 - \Delta^2(T)}} dE\right]. \tag{1.11}$$

Thus, the normalized stiffness for s-wave pairing is:

$$\frac{\lambda_L^{-2}(T,\Delta_0)}{\lambda_L^{-2}(0,\Delta_0)} = 1 + 2\int_{\Delta(T)}^{\infty} \partial_E f \cdot \frac{EdE}{\sqrt{E^2 - \Delta^2(T)}}, \tag{1.12}$$

where Δ_0 is the gap at $T = 0$, E is quasiparticle energy, f is the Fermi-Dirac distribution.

The temperature dependence of Δ can be found self-consistently from [8]:

$$\int_0^{\infty} dE\left[\frac{\tanh\left(\frac{1}{2k_BT}\sqrt{E^2+\Delta^2}\right)}{\sqrt{E^2+\Delta^2}} - \frac{1}{E}\tanh\left(\frac{E}{2k_BT_c}\right)\right] = 0. \tag{1.13}$$

An approximate form for the s-wave temperature dependence is [9]:

$$\Delta(T) = \Delta_0 \tanh\left\{1.821\left[1.018\left(\frac{T_c}{T} - 1\right)^{0.51}\right]\right\}. \tag{1.14}$$

For a system with two s-wave gaps, the total stiffness can be written as [10]:

$$\rho_T(T) = w\rho_{\Delta_1}(T) + (1-w)\rho_{\Delta_2}(T). \tag{1.15}$$

1.1.4 Thin films

Thin-film superconductors with $d \ll \lambda_L$ (where d is the film thickness) differ in the characteristic length scale governing magnetic field penetration. Instead of λ_L which accounts for the exponential decay of magnetic fields in bulk, a two-dimensional superconductor exhibits a power-law decay over the characteristic length scale

$$\Lambda = \frac{2\lambda_L^2}{d}, \tag{1.16}$$

known as the Pearl length [11].

1.2 Vortices in Type II Superconductors

Type II superconductors exposed to magnetic fields between H_{c1} and H_{c2} allow magnetic flux to penetrate in quantized units,each of size $\Phi_0 = \frac{2\pi\hbar}{e^*}$ called the superconducting flux quantum [1]. This results in the formation of vortex lines with normal-state cores surrounded by circulating supercurrent that screen the magnetic field over λ_L.

These vortices interact with the superfluid,exert forces on each other, and can arrange themselves into ordered lattices structures in clean superconductors.

1.2.1 Forces acting on vortices

The motion of vortices in type II superconductors is influenced by randomly distributed pinning sites in the crystal lattice, and several distinct forces [12]:

- Lorentz force: $f_L = \Phi_0 J \times \hat{n}$ - arising from the interaction of the supercurrent $\vec{J}$ with the normal core. here, $\hat{n}$ is the unit vector parallel to the applied magnetic field.

- Viscous force: $f_\eta = \eta \vec{v_v}$ - the viscous drag due to dissipation in the core, described by the Anderson-Kim model. here η is the viscosity coefficient and $\vec{v}_v$ is the vortex velocity.

- Magnus force: $f_M = \rho_s \Phi_0 \Delta\vec{v} \times \hat{n}$ - resulting from the relative velocity between the supercurrent and the vortex, $\Delta\vec{v} = \vec{v}_s - \vec{v}_v$ where $\vec{v_s}$ is the superfluid velocity and $\vec{v_v}$ is the vortex velocity.

- Hall force: $f_H = \alpha_l \vec{v}_v \times \hat{n}$ - due to the transverse response of quasiparticles bound to the moving vortex core. here α_l is the Hall coefficient.

The net force acting on a vortex, along with the random pinning force, can pin or depin vortices from pinning sites.

1.2.2 Collective pinning of a single vortex in a random potential

Pinning a vortex in space can occur either due to a strong pinning center or due to the collective interaction between the vortex and a large number of randomly distributed weak pinning centers. The vortex can be modeled as an elastic string, with the coordinate along the string denoted by z, and transverse displacements by $u(z)$. Each segment of length L_c (The Larkin length) is pinned independently.

1.2.3 Collective pinning of vortex bundles

Abrikosov showed that in the ultra clean limit, vortices form a triangular lattice [13]. In this case, the vortex lattice may be treated as an elastic medium with elastic moduli: c_{11} (compression), c_{44} (tilt), c_{66} (shear), these constants control the distortions on the lattice in response to forces acting on it. In the presence of pinning centers, quenched disorder distorts the vortex lattice to minimize the total free energy. In the case the nucleation sites are weak and unable to pin the vortices individually, the vortices are instead pinned collectively.

1.2.4 Dew-Hughes classification

Dew-Hughes proposed a scheme to distinguish pinning by extended and point-like defects by treateing the lattice elastically, imposing a defect as a perturbation, and computing the resulting energy change. Explicitly, using the reversible magnetization (i.e., the ultra-clean limit), one uses the relation

$$f_{\text{pin}} = \frac{\Delta W}{x} = -\frac{\phi_0 \Delta M_{\text{rev}}}{x} \tag{1.17}$$

where f_{pin} is the force per unit length on a pinned flux line, W is the work done by the driving force, x is the effective pinning interaction range, and M_{rev} is the reversible component of the magnetization [14].

1.2.5 Electrodynamic equations of flux creep

Vortices in type II superconductors experience a Lorentz force due to the screening supercurrent, which induces their motion. The motion of vortices generates an electric field antiparallel to the supercurrent, leading to energy dissipation known as flux creep. To describe this behavior, we use Maxwell's equations together with the electric field induced by vortex [15]:

$$\vec{\nabla} \times \vec{E} = -\partial_t \vec{B}, \tag{1.18}$$

$$\vec{\nabla} \times \vec{B} = \mu_0 \vec{J}, \tag{1.19}$$

$$\vec{E} = \vec{v} \times \vec{B}, \tag{1.20}$$

where $\vec{E}$ is the electric field and $\vec{v}$ the vortex velocity. Together, these equations govern dissipation in the superconductor. In a simplified model, the time dependence of the supercurrent can be written as:

$$\mu_0 \partial_t J = \partial_x^2 (vB), \tag{1.21}$$

1.2.6 Depinning through thermal activation

A Vortex pinned in a shallow potential can be thermally deppinned, and the resulting flux creep is described by [15]:

$$J = J_{\text{depin}}(1 - \frac{k_B T}{U_0} \ln\left(\frac{t}{\tau}\right)) \tag{1.22}$$

where J_{depin} is the depinning current, k_B is the Boltzmann constant, U_0 is the pinning barrier, t is time, and τ is the characteristic depinning attempt time.

1.3 Paramagnetism and Ferromagnetism

Magnetic susceptibility χ characterizes the linear response of the magnetization M to an applied magnetic field H:

$$M = \chi H \tag{1.23}$$

Different microscopic mechanisms can produce a magnetic response, and the functional form of χ reflects these mechanisms:

1.3.1 Paramagnetism

In paramagnetic materials, atoms possess randomly oriented magnetic moments due to the orbital and spin angular momentum of unpaired electron. When exposed to an external field, the moments partially align parallel to the field, resulting in net magnetization proportional to the applied field. Thermal fluctuations oppose alignment, leading to a diminished net response. The Curie-Weiss law describes this response [16]:

$$\chi = \frac{C}{T - T_c} \tag{1.24}$$

where $C = \frac{\mu_0 \mu_B^2 N g^2 J(J+1)}{3k_B}$ is the Curie Constant and T is the temperature, T_c (θ for paramagnets) is the Curie temperature μ_0 is the vacuum permeability, μ_B is the Bohr magneton, N is the number of magnetic ions, g is the lande g-factor, and J is the total angular momentum. For weak interaction between moments, the Curie temperature is small ($T_c \to 0$).

1.3.2 Ferromagnetism

In ferromagnetic material, neighboring moments interact strongly through the exchange field. This interaction favors parallel alignment of neighboring spins leading to spontaneous long range order below T_c. Below T_c the net magnetization remains finite even in the absence of applied external magnetic field. This results in a finite Curie temperature in the Curie-Weiss law.

1.4 $FeSe_{0.5}Te_{0.5}$

1.4.1 Structure

Iron-based superconductors are a class of high-T_c superconductors. FeSe belongs to the iron-Chalcogenide family and has a simple tetragonal PbO structure. By substituting selenium (Se) with tellurium (Te), two significant effects emerge due to increased spin-orbit coupling (SOC) and changes to the electronic and crystal structure (aside from the nematicity seen in [17]): an increase in the superconducting T_c, and the emergence of nontrivial topology in the electronic band structure [2].

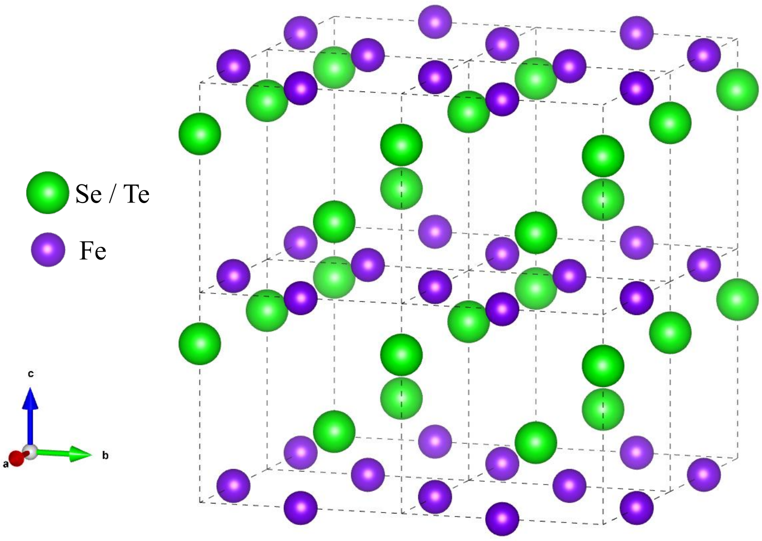

Figure 1.2: The crystal structure of $FeSe_{0.5}Te_{0.5}$.

Figure 1.2 shows the crystal structure of $FeSe_{0.5}Te_{0.5}$ each unit cell is outlined with dashed lines, iron atoms are purple and chalcogen atoms (Se/Te) are green. Se and Te occupy similar sites, with small deviations observed in [18]). Figure adapted from [5] and constructed using [19].

1.4.2 Topology

Density-functional-theory (DFT) calculations predict two electron pockets around the M point, two hole bands near the Γ point, and band inversion in $FeSe_{0.5}Te_{0.5}$ [20, 21]. Two superconducting gaps were reported in [22], while angle-resolved photoemission spectroscopy (ARPES) has confirmed the predicted band inversion in normal state $FeSe_{0.45}Te_{0.55}$ [4]. This band inversion is responsible for the material's nontrivial topology, specifically the topologically protected surface states in the superconducting phase [2, 23]. The complex low energy electronic structure also allows for unconventional pairing, such as s+id, which could spontaneously break time-reversal symmetry (TRS), as suggested in [2]and supported by [23].

1.4.3 Superconductivity

Several experimental techniques have been used to investigate the superconducting and topological properties of $FeSe_{0.5}Te_{0.5}$. Muon-spin spectroscopy (μSR) has been used to characterize λ_L and ρ_s, supporting a nontrivial pairing mechanism and probing the possible spontaneous breaking of time-reversal symmetry [23]. Scanning tunneling microscopy (STM) has been used to determine the coherence length ξ and to probe possible Majorana zero modes in vortex cores and at edges [24, 25]. using SnS-Andreev spectroscopy and H_{c1} measurements [22], the two superconducting gaps were measured.

1.4.4 Pinning Regimes

Pinning mechanisms have been characterized extensively in $FeSe_{0.5}Te_{0.5}$ tapes [26], in bulk [27], and in films grown on substrates such as LAO and STO with $d = 100, 200$(nm) [28], where I-V characteristics were measured with and without an applied field, revealing a field-dependent shift in the pinning regimes, STM imaging reveals many screw dislocations, yet all of these characterizations showed no temporal dependence of current or magnetization.

Chapter 2

Stiffnessometer

The Stiffnessometer is an experimental setup designed to measure the superconducting stiffness, ρ_s, and the superconducting coherence length, ξ. The setup consists of a superconducting annulus, placed concentrically around a long (ideally infinite) excitation coil. Driving a DC current in the excitation coil threads magnetic flux through the annulus. The annulus is subjected to a magnetic vector potential, $\vec{A}(r) = \frac{\Phi_{EC}}{2\pi r} = \frac{\mu_0 n I R^2}{2r}\hat{\varphi}$ (outside a long solenoid of radius R) without being directly exposed to H, so supercurrents are induced (Meissner effect) [29, 6, 5]. Two main measurement protocols are available:

Step	Action
1	Reach the desired base temperature.
2	Drive desired current in excitation coil.
3	Measure the magnetic moment.

Table 2.1: ZGFC protocol – Cooling to the desired temperature, drive a current in the excitation coil, and measure the moment.

The Zero-Gauge-Field Cooling (ZGFC) protocol sets $\vec{\nabla}\phi = 0$ in the London equation (i.e., fixes the gauge).

Step	Action
1	Drive desired current in excitation coil.
2	Reach the desired base temperature.
3	Extinguish (null) the current in the excitation coil.
4	Measure the magnetic moment.

Table 2.2: GFC protocol – drive current in the excitation coil, cool to the desired temperature, set the current in the excitation coil to zero, and measure the moment.

The Gauge-Field-Cooling (GFC) protocol sets the gauge-invariant combination to zero in the London equation $\vec{A}_{tot} - \frac{\Phi_0}{2\pi}\vec{\nabla}\phi = 0$.
The applied magnetic vector potential generates currents in the annulus which themselves produce a magnetic moment, we measure this moment using a superconducting quantum interference device (SQUID) magnetometer. The linearity of the London

equation allows us to distinguish between a linear-response regime and a nonlinear-response regime, the transition occurs when the excitation-coil current reaches a critical value $I = I_c$.

2.1 Obtaining ξ

To obtain ξ, we start from Equation 1.7 under a thin-ring approximation (the ring's self magnetic vector potential is negligible compared with that of the excitation coil). Using the symmetry of the problem, we assume a separable order parameter solution that minimizes free energy $\Psi = \psi(r)\Theta(\theta)$ with ψ approximately constant across the ring's width, and obtain the relation between the critical flux and ξ [6]:

$$\frac{\Phi_c}{\Phi_0} \approx \frac{r_{out}}{\xi} \tag{2.1}$$

2.2 Obtaining λ

We start from the two-dimensional form of Equation 1.1. Using Ampere's law and $\vec{B} = \vec{\nabla} \times \vec{A}$, we obtain:

$$\vec{\nabla} \times \left(\vec{\nabla} \times \vec{A}_{SC}\right) = -\mu_0 \rho_s \vec{A}_T \tag{2.2}$$

$$\nabla \left(\overbrace{\vec{\nabla} \cdot \vec{A}_{SC}}^{0} \right) - \nabla^2 \vec{A}_{SC} = -\mu_0 \rho_s \vec{A}_T \tag{2.3}$$

$$\nabla^2 \vec{A}_{SC} = \mu_0 \rho_s \left(\vec{A}_{SC} + \vec{A}_{EC}\right) \tag{2.4}$$

$$\nabla^2 \vec{A}_{SC} = \mu_0 \rho_s \left(\vec{A}_{SC} + \frac{\Phi_{EC}(R_{pl})}{2\pi r}\hat{\varphi}\right) \tag{2.5}$$

$$\frac{\partial^2 A}{\partial^2 z} + \frac{\partial^2 A}{\partial^2 r} + \frac{1}{r}\frac{\partial A}{\partial r} - \frac{A}{r^2} = \frac{1}{\lambda^2}\left(\vec{A} + \frac{1}{r}\hat{\varphi}\right) \tag{2.6}$$

where in line 2.3 we used vector identities, in line 2.4 we choose the London gauge, in line 2.5 we substitute the vector potential of an long solenoid, and in line 2.6 we exploit cylindrical symmetry and normalize variables as: $\frac{r}{R_{pl}} \to r$, $\frac{A_{SC}}{A_{EC}(R_{pl})} \to A$, $\frac{\lambda}{R_{pl}} \to \lambda$. This gives the strong formulation of the PDE. We then convert it to the weak formulation (multiply by a test function and integrate by parts) and solve with FreeFEM++ to obtain the vector potential at the pickup loop, $A(R_{pl})$, as function of λ.

The normalized A is given by:

$$A(R_{pl}) = \frac{A_{SC}(R_{pl})}{A_{EC}(R_{pl})} = \frac{\frac{\mu_0 m}{4\pi R_{pl}}}{\frac{\mu_0 n I R_{EC}^2}{2R_{pl}}} = C \cdot \frac{m}{I} \tag{2.7}$$

where C is a calibration constant that can be calculated from the geometry or obtained directly from measurement.

This means that from the linear $\frac{m}{I}$ response we can directly retrieve $A\left(R_{pl}\right)$.

Chapter 3

DC Field measurements

The Zero-Field-Cool (ZFC) protocol proceeds as follows:

Step	**Action**
1	Reach $T = 15\,\mathrm{K}$.
2	Null the applied field.
3	Reach the desired base temperature.
4	Reach the desired field.
5	Measure the moment as a function of time.

Table 3.1: ZFC protocol – Heating to $15\,\mathrm{K}$, null the applied field, cool to the base temperature, apply the desired field, and measure the magnetic moment.

This protocol ensures that no magnetic flux is trapped in the sample and minimizes the influence of sample history.
The Field-Cool (FC) protocol proceeds as follows:

Step	**Action**
1	Reach $T = 15\,\mathrm{K}$.
2	Reach the desired field.
3	Reach the desired base temperature.
4	Measure the magnetic moment as a function of time.

Table 3.2: FC protocol – Heat to $15\,\mathrm{K}$, apply the desired field, cool to the base temperature, and measure the magnetic moment.

While this protocol can retain some history effects (since flux dynamics can influence subsequent time steps from the onset of superconductivity), maintaining constant cooling rate allow us to distinguish between the equlibrium superconducting state (set by temperature and applied field) and history effects. This minimizes the influence of earlier protocol iterations on the current combination of applied field and temperature.

Chapter 4

System Setup

A thin superconducting film was deposited on an annular $LaAlO_3$ (LAO) substrate, and a long excitation coil threads the center of the annulus.

Both components are placed inside a Quantum Design MPMS3 SQUID magnetometer equipped with an external coil capable of nulling the field or applying an external field.

By generating a magnetic vector potential - either curl-free field using the excitation coil or one with a finite curl using the external coil - we measure the resulting flux with a SQUID magnetometer.

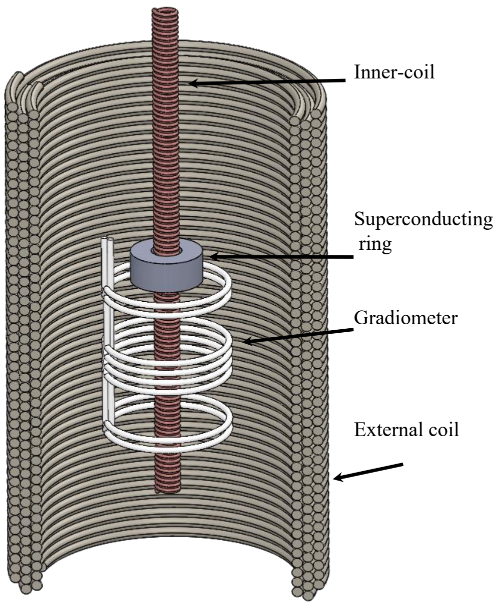

Figure 4.1: Schematic of the MPMS3 in Stiffnessometer configuration. Depicted are the ring and excitation coil (”inner coil”), a second order gradiometer (connected to a SQUID, not shown), and an external coil for field nulling or external field application.

Figure 4.1 shows the MPMS3 in the Stiffnessometer configuration. The ring is threaded by an excitation coil (marked ”inner coil” in the figure). Outside the ring is a second-order gradiometer (connected to a SQUID, not shown in Figure 4.1). These are surrounded by an external coil for field nulling or external-field application (in practice, the MPMS3 contains two external coils: one for field nulling and another for applying an external field). The SQUID is then connected to a second-order gradiometer in our setup, meaning the setup relates the flux through the gradiometer loop to a voltage (via the SQUID electronics), allowing us to scan along the z-axis (parallel to the excitation coil and normal to the plane of the annulus) and map the flux profile. We do this in two main modes:

DC mode - This mode measures the sample's magnetic moment by moving it along the axis normal to ring's surface. The MPMS3 records the flux threading the second-order gradiometer and converts it into a voltage. This voltage response is then fitted to the theoretical profile of an induced dipole, from which the magnetic moment is determined.

VSM mode - Similar to DC mode, the sample is moved along the same measurement axis, however, in this mode it is mechanically oscillated with a defined amplitude and frequency. The resulting oscillating voltage is recorded and fitted to a theoretical response profile of a magnetic moment, from which the moment is extracted.

Measurements performed using VSM and DC modes yield similar results, therefore we use both methods interchangeably unless specified otherwise.

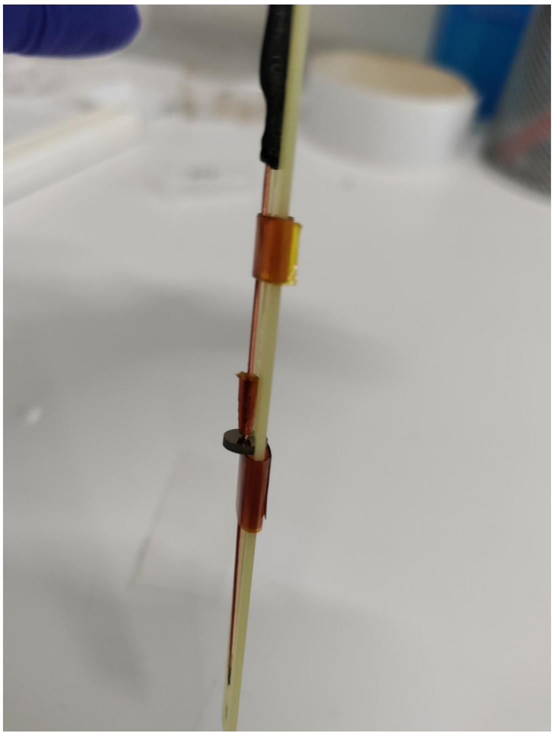

Figure 4.2: Sample-holder assembly used in the Stiffnessometer experiment. The holder consists of a copper excitation coil threading the superconducting ring and an LAO substrate with the $Fe_ySe_xTe_{1-x}$ film.

In Figure 4.2 the Stiffnessometer sample holder is shown. It consists of two main components: a copper excitation coil that threads the ring, and an LAO substrate with FeSeTs film deposited on top (the ring). In practice an additional support piece is used to secure the ring's position. The response of the setup above T_c is referred to as background (BG) and subtracted from the measured signal when explicitly mentioned.

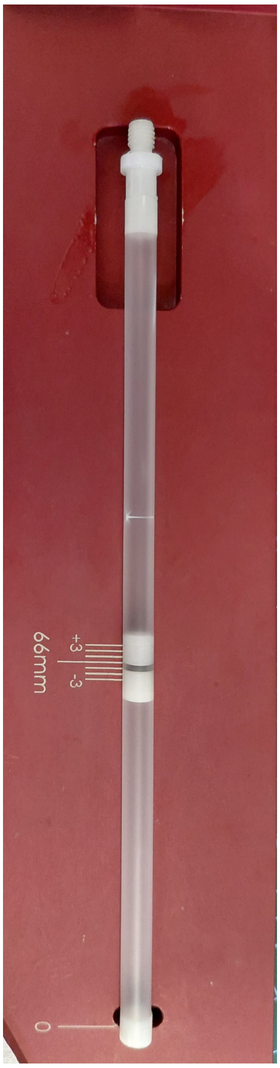

Figure 4.3: Sample holder used for external field measurements. The setup consists of a straw-bead assembly securing the superconducting ring.

In Figure 4.3, the sample holder used for external field measurements is shown. It consists of two main components: the holder assembly (a straw and beads that secure the ring's position) and the superconducting ring (as depicted above). The response of the holder with a bare LAO substrate is recorded for each field and temperature combination and is referred to as the background (BG). This BG is subtracted from the measured data whenever explicitly indicated.

4.1 SQUID Magnetometer

The Superconducting Quantum Interference Device (SQUID) is an extremely sensitive detector of magnetic flux. A DC SQUID, as used in our setup, is composed of a two halves of a superconducting loop separated by two non-superconducting segments (two Josephson junctions).

The critical current in the SQUID is modulated by the applied flux as:

$$I_c(\Phi) = 2I_{c0} \left| \cos\left(\frac{\pi\Phi}{\Phi_0}\right) \right| \tag{4.1}$$

By integrating changes in the measured signal, the total flux threading the SQUID can be reconstructed.

Chapter 5

Experimental results

5.1 Magnetic response

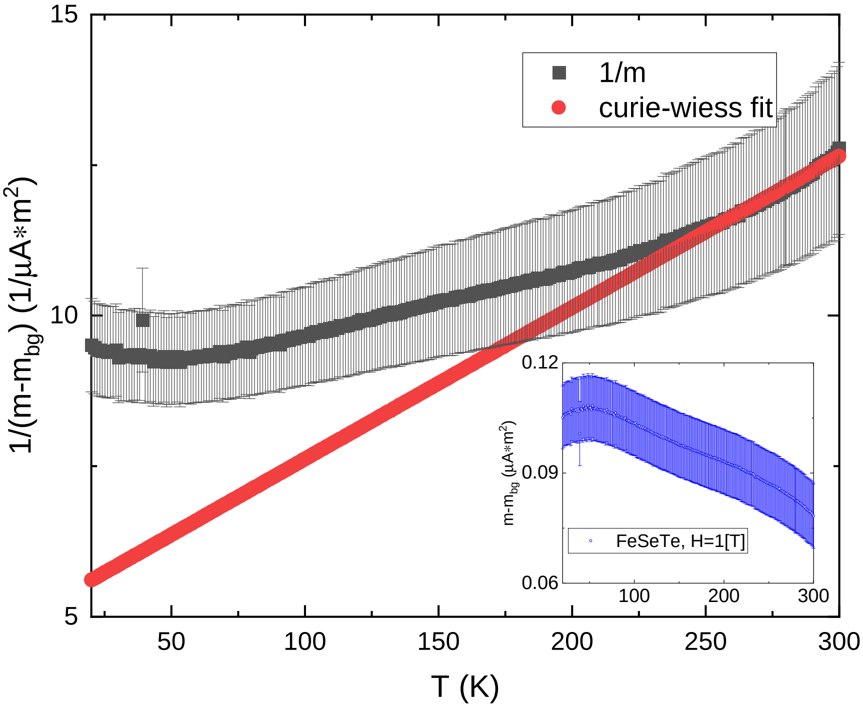

Figure 5.1: Magnetic response of an $Fe_ySe_xTe_{1-x}$ film grown on an LAO substrate measured as a function of temperature under a constant applied field of $H = 1$ (T). The LAO substrate response was measured separately and subtracted to isolate the film contribution (inset). The main panel shows the inverse magnetization as a function of temperature, compared with the expected Curie–Weiss behavior. The measured data (black squares) deviate from the linear Curie-Weiss fit (red circles), indicating that the response does not follow the Curie-Weiss law and is likely not attributable to excess iron in the film.

The magnetic response of $Fe_ySe_xTe_{1-x}$ film grown on an LAO substrate was measured as a function of temperature under a constant field of $H = 1$ (T), alongside measurements of a bare LAO substrate. By subtracting the substrate contribution we obtain the film's intrinsic response as a function of temperature, shown in the inset of Figure 5.1. The maximum magnetic signal was on the order of $0.1\mu A \cdot m^2$. Notably the response does not follow the expected Curie-Weiss behavior. This is evident in Figure 5.1, where the inverse magnetization is plotted as a function of temperature: instead of the expected linear dependence (red circles) the measured data (black squares) deviate significantly. Fitting the steepest part of the curve (250K-300K) yields an effective Curie-Weiss temperature $T_c = -154K$, which corresponds to an antiferromagneitc response (rather than a ferromagnetic or even paramagnetic). However, since the overall behavior fails to conform to the Curie-Weiss law, we cannot attribute the dominant measured response to excess iron in the film and therefore disregard this contribution in further analysis.

5.2 Stiffnessometer

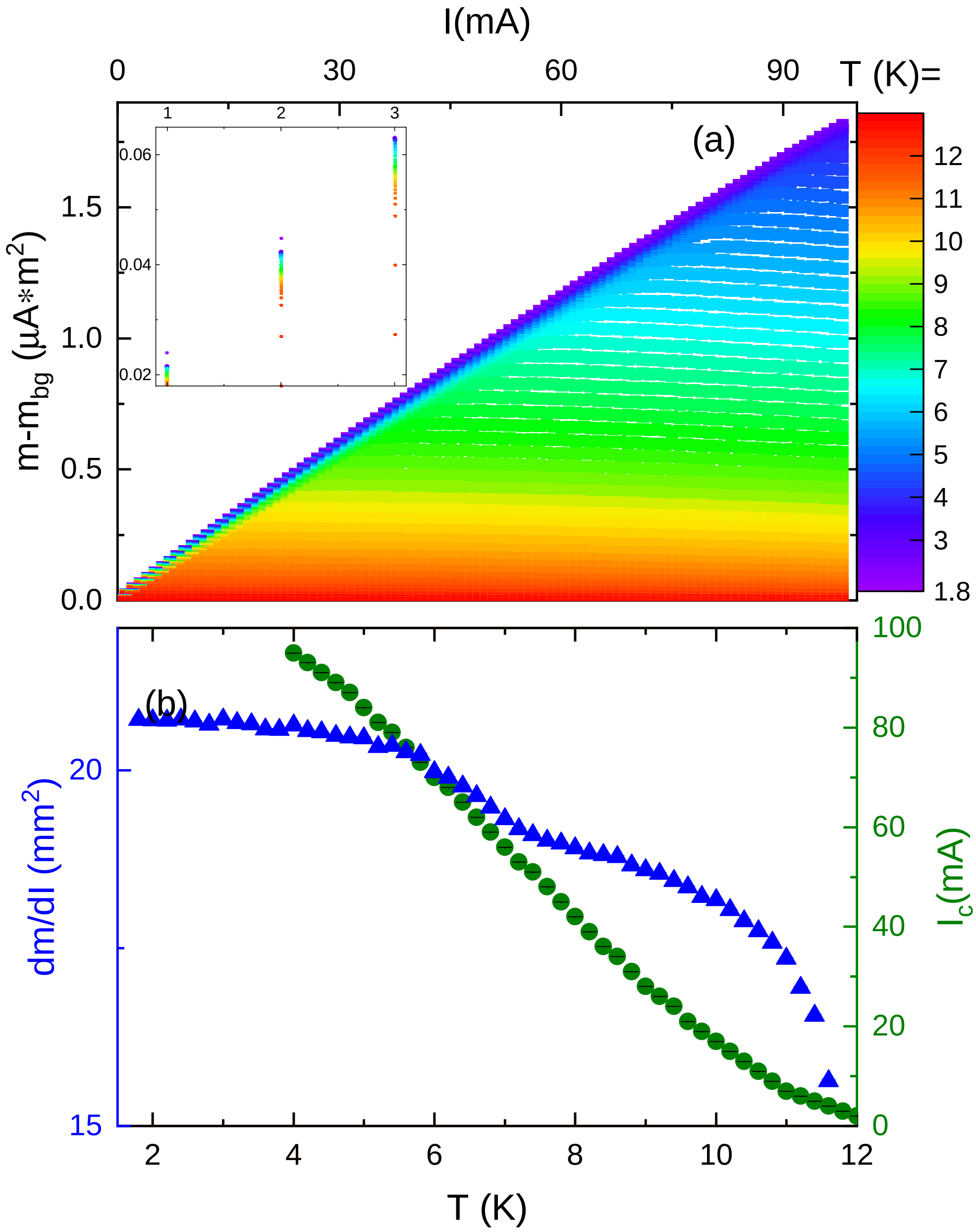

Figure 5.2: (a) Excitation coil current dependence of the subtracted magnetic moment at various temperatures (color bar). At low currents a linear relation is observed, above a critical current the response saturates to a plateau. The low current response is isolated to highlight the knee in the dM/dI response (inset). (b) Temperature dependence of the low currents linear slope (blue triangles) and of the critical currents (green circles).

Figure 5.2(a) shows the excitation coil current dependence of the subtracted magnetic moment for a range of temperatures, indicated by the color bar. At low currents the response is linear, above a critical current the magnetic moment saturates into a plateau. The linear response at low currents shows two pronounced features: a change in slope around 7K, and a more pronounced change near T_c. From these measurements we extract two quantities: the slope of the low current linear response, and the critical current marking the onset of the plateau. Their temperature dependence is presented in Figure 5.2(b). The slope values (blue triangles) decrease monotonically with temperature and first exhibit a knee around 7K , followed by a pronounced drop near T_c. In contrast, the critical current values (full green circles) follow a smoother trend and vanish gradually as T approaches T_c. We note that, at time of fabrication, T_c was reported to be $T_c \approx 13K$ a decrease of 7.6%, which can be attributed either to sample degradation due to atmospheric exposure or to measurement resolution limitations.

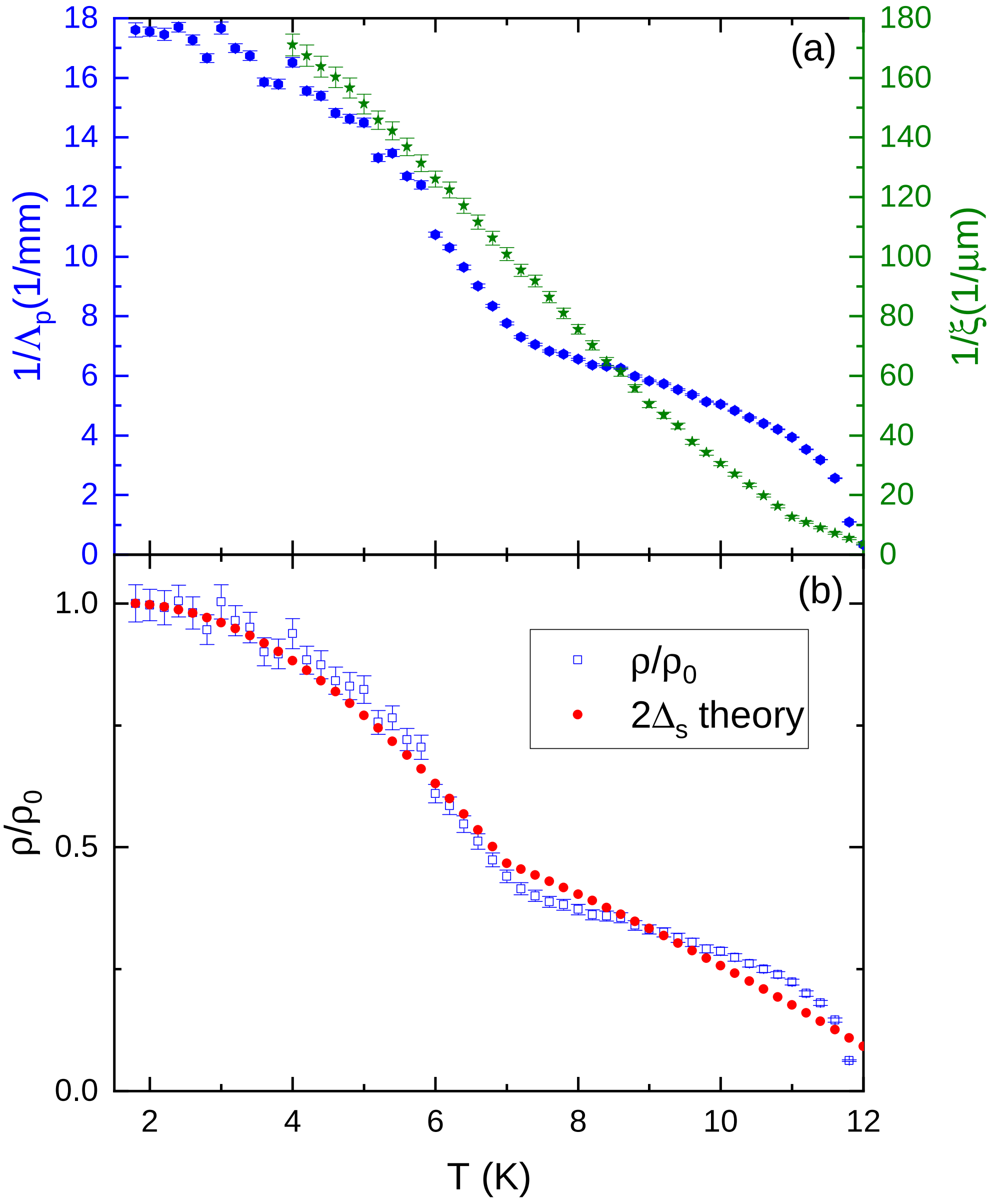

Figure 5.3: (a) Temperature dependence of the inverse Pearl length Λ_p^{-1} (blue circles) and the inverse coherence length ξ^{-1} (green full stars). Λ_p^{-1} shows a pronounced knee around 7(K) and vanishes at T_c, , while ξ^{-1} evolves smoothly. (b) Normalized superfluid stiffness (open blue squares) compared with the two-gap s-wave model (filled red circles) with $T_c = 13.4K$. The model reproduces the overall temperature dependence and the two-gap structure, with extracted parameters $T_{c,1} = 13.4, (\mathrm{K})$, $T_{c,2} = 7, (\mathrm{K})$, $\Delta_1 = 2.04\mathrm{meV}$, $\Delta_2 = 1.06\mathrm{meV}$, and weight $w = 0.57$, but deviates close to $T = 12(\mathrm{K})$.

The temperature dependence of the inverse Pearl length, Λ_p^{-1}, was obtained by solving the London Equation 1.1 under the Coulomb gauge for a 2D annulus using FreeFEM++ [29, 30], we then retrieve the Pearl length Λ_L as explained in section 2.2, and using Equation 2.1 as explained in section 2.1 we extracted ξ.

The extracted values, shown in Figure 5.3(a) as blue circles, decrease monotonically with increasing temperature, displaying a pronounced "knee" around 7(K) and vanishing at T_c. Note that the uncertainties increase towards low temperature because the Λ_p vs. $\frac{dm}{dI}$ curve plateaus. The inverse coherence length ξ^{-1}, extracted independently from the break in the linear response of $\frac{m}{I}$ using Equation 2.1 and plotted as green full stars in Figure 5.3(a), also decreases monotonically but follows a smoother temperature evolution without a visible knee. From the experimentally determined Λ_p we extracted the London penetration depth, λ_L, using Equation 1.16. Using the approximate temperature dependence of the superconducting gap Equation 1.14 and numerically evaluating Equation 1.12 we obtained the normalized superfluid stiffness for a two gap s-wave model. Figure 5.3(b) shows the measured normalized stiffness (empty black squares) together with the two-gap theoretical curve (full red squares). Assuming $T_c = 12$(K) the theoretical model captures the overall temperature dependence and the characteristic two-gap structure, though deviations appear near T_c. From the fit we extract $T_{c,1} = 12$(K), $T_{c,2} = 7$(K), corresponding to gap values of $\Delta_1 = 1.82$meV and $\Delta_2 = 1.063$meV, with a relative weight $w = 0.68$. In comparison, [22] reported $\mathrm{T}_{c,\mathrm{SNS}} = 14$(K) with gaps $\Delta_{1,\mathrm{SNS}} = 3.3 - 3.4$meV and $\Delta_{2,SNS} = 1meV$. While $\Delta_{2,SNS}$ agrees with our findings, $\Delta_{1,SNS}$ is 81-86% larger than our Δ_1 (for $T_c = 12(K)$). We note that the measured $\mathrm{T}_{c,SNS} = 14K$ is 16% greater than our measured T_c and the SNS values were obtained on bulk single crystal, and we note the limitations of the applied model that assumes negligible coupling between the gapped bands. Allowing $T_c > 12$(K) the two-gap fit yields $T_c = 13.4$ K with $w = 0.57$ and $\Delta_2 = 2.065$ meV, in better agreement with the T_c reported by the fabricators, as seen in Figure 5.3. This may indicate that, although the system is superconducting (Cooper pairing present), our measurement sensitivity limits prevent resolving the full response near T_c.

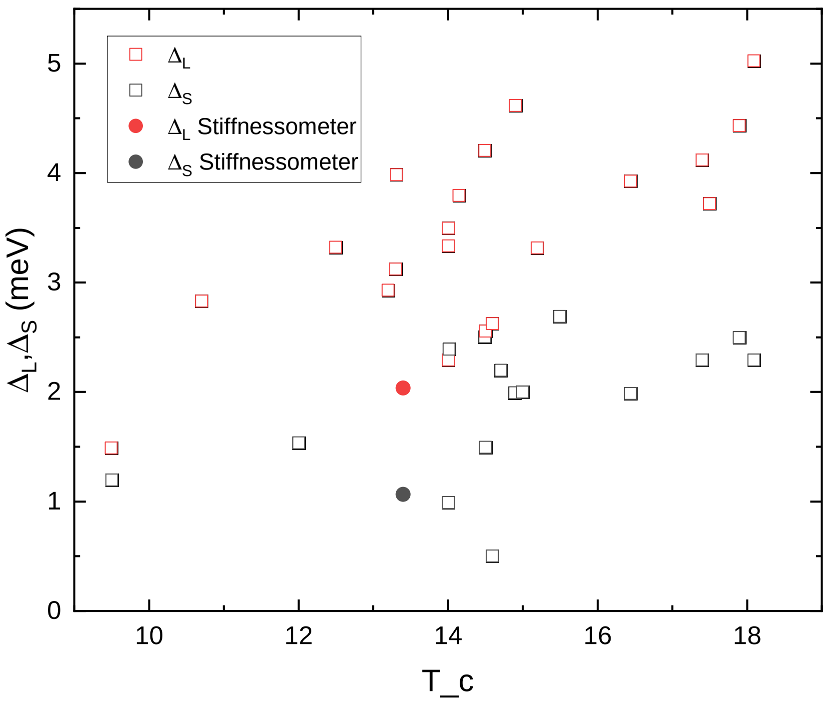

Figure 5.4: Superconducting gap magnitudes Δ_L and Δ_s in $Fe_ySe_xTe_{1-x}$ samples plotted as a function of the measured T_c.The figure is adapted from [22]; the original work reports two general linear trends for the large and small gaps but does not differentiate between bulk and thin-film samples, single-crystal versus polycrystalline forms, or deviations from the target stoichiometry in x and y. The two colored circular markers represent the gaps extracted from the present stiffnessometer measurements. Partial agreement with the trends of [22] is observed, which is plausibly due to the use of a model that assumes negligible interband coupling.

To compare this work's measurements with established trends in $Fe_ySe_xTe_{1-x}$ Figure 5.4 show the adapted gap sizes vs. T_c diagram from [22] and overlaid the gap values extracted from stiffnessometer analysis (shown as the two full-color circular markers). [22] reports two broad linear trends corresponding to the small and large superconducting gaps but does not distinguish between single-crystal and polycrystalline samples, between bulk and film geometries, or variations arising from deviations in the actual stoichiometry of x and y. When placed on the same diagram, my data points follow the qualitative behavior of the reported Δ_L and Δ_S trends, though with noticeable deviations. This partial agreement is likely connected to the simplifying assumption in my modeling that the superconducting bands are uncoupled. The model therefore cannot capture effects arising from interband pairing, which are believed to be relevant in $Fe_ySe_xTe_{1-x}$ systems.

To obtain an independent consistency check of the extracted coherence length ξ and penetration depth λ, we used these values to compute the temperature dependence of the lower critical field $H_{c1}(T)$ using Equation 1.6:

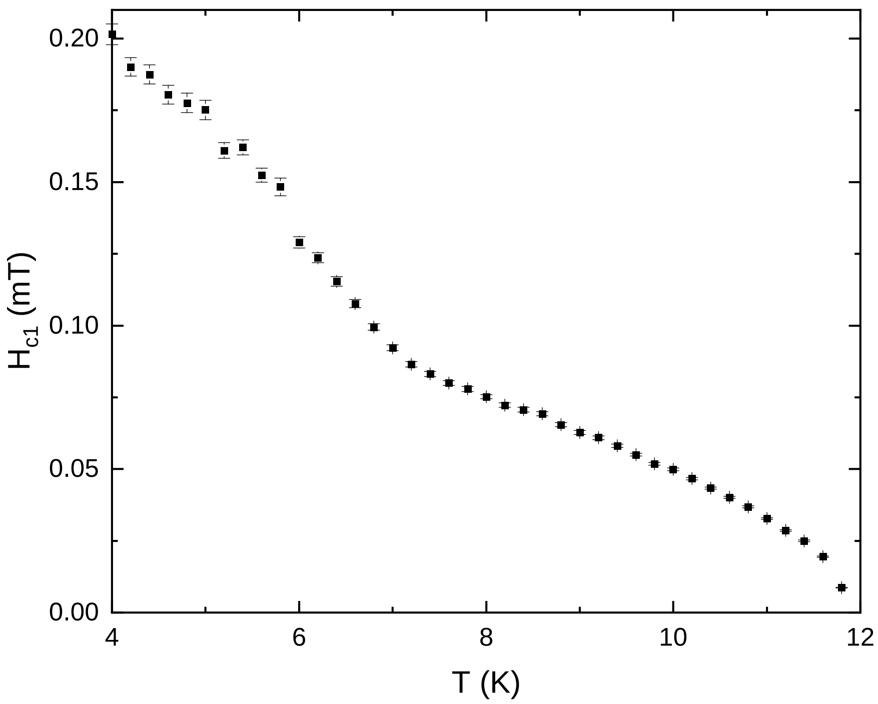

Figure 5.5: Temperature dependence of H_{c1} extracted using Equation 1.6. The data show a monotonic decrease of H_{c1} as temperature increases, with a visible knee feature that corresponds to the anomaly observed in λ_L(T). The absolute values of H_{c1} fall in the mT range.

Figure 5.5 presents the temperature dependence of H_{c1}, obtained using Equation 1.6. As expected for a type-II superconductor, H_{c1} decreases monotonically with temperature. A noticeable knee appears near the same temperature at which we observed a deviation in $\lambda_L(T)$ supporting the internal consistency of the analysis. Note that the extracted values lie within the mT regime.

Independent measurements using FC and ZFC protocols, as presented in Table 3.1 and Table 3.2, were later performed to verify these values as seen in Figure 5.7 and Figure 5.11. The corresponding results, reveal an unexpected time dependence, highlighted in Figure 5.6.

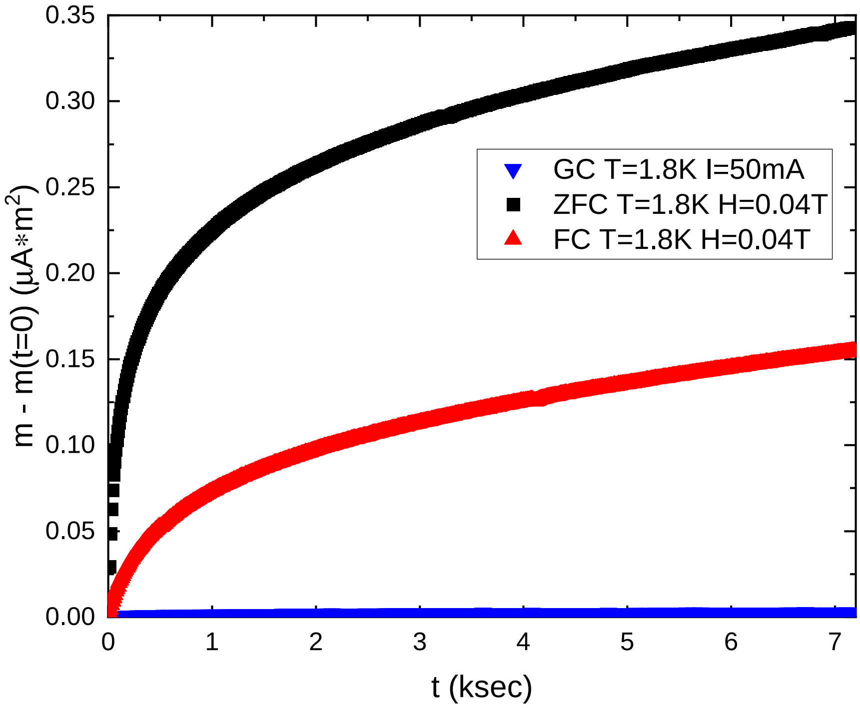

Figure 5.6: Time dependence of the magnetization relative to its initial value for Zero Field Cool (ZFC, black squares) Field Cool (FC, red upward triangles) and Gauge Cool (GC, blue downward triangles) measurements. ZFC and FC exhibit a clear positive, nonlinear change in magnetization over time, while GC show only a negligible increase.

Figure 5.6 presents the time dependence of the magnetization relative to its initial value for for Zero field Cool (ZFC, black squares) Field Cool (FC, red upward triangles) and Gauge Cool (FC, blue downward triangles). Both the ZFC and FC cases exhibit a clear positive change in magnetization over the measured time interval, whereas the GC response shows only a negligible positive change. in addition, the ZFC and FC curves display a show a non-linear time dependence.

5.3 Geometric effect

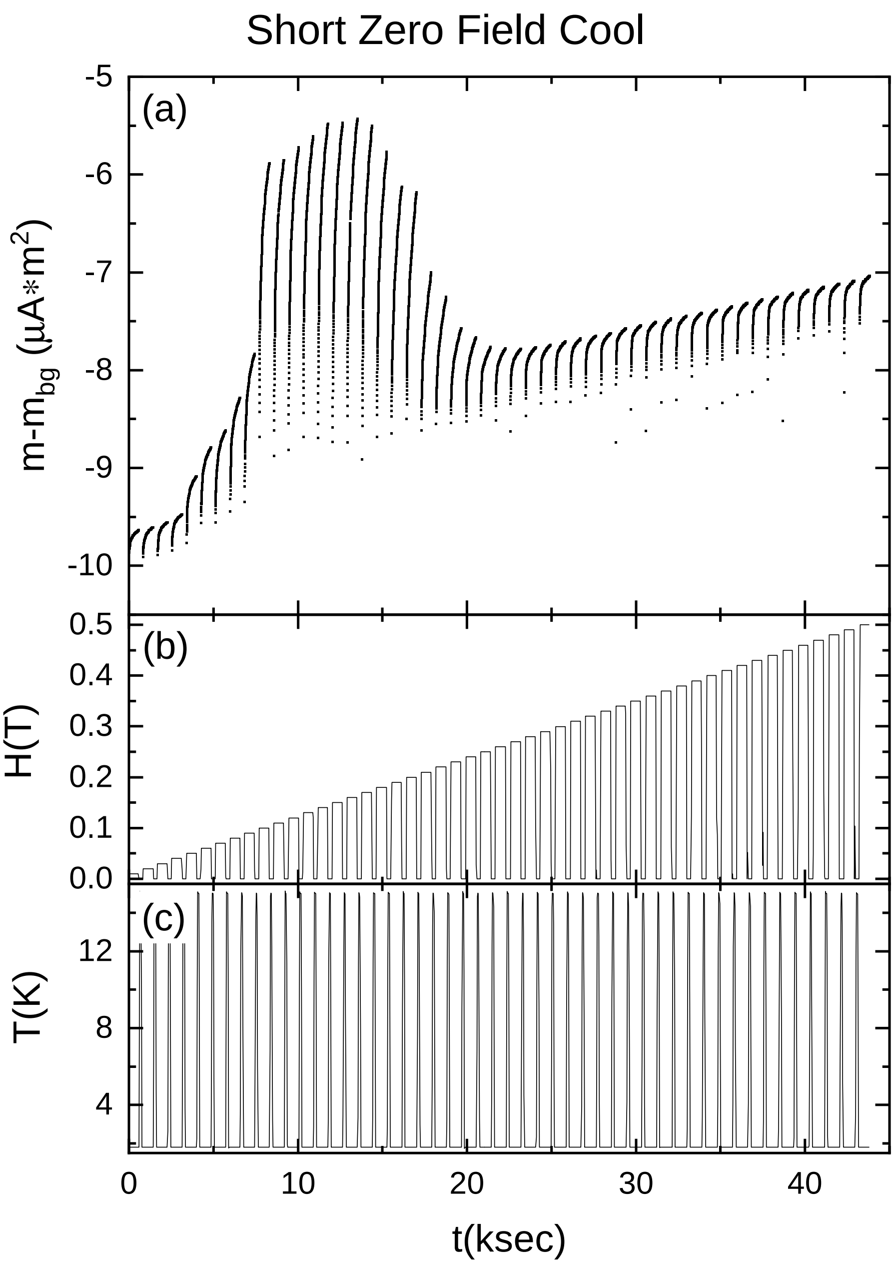

Figure 5.7: Time dependence of the subtracted magnetic moment of the $Fe_ySe_xTe_{1-x}$ film under the zero-field cooling (ZFC) protocol at a base temperature of $T = 1.8$ (K) during a short time period of 0.6 $(ksec)$. The protocol (outlined in Table 3.1) prevents flux trapping and eliminates sample history effects. In (a) the reduced magnetic moment exhibits an initial nonlinear increase with applied field up to $H \approx 0.1$ (T), a further unsaturated growth up to $H \approx 0.2$ (T), and then approaches saturation as the field increases beyond this field and toward $H = 0.5$ (T). Panels (b) and (c) show the field and temperature vs. time respectively.

Figure 5.7 (a) shows the subtracted magnetic moment (i.e. the measured moment of the $Fe_ySe_xTe_{1-x}$ film with the substrate minus the substrate's magnetic response) as a function of time, for a constant base temperature $T = 1.8$ (K) in the zero field cool protocol over 0.6 $(ksec)$. Figure 5.7 (b) and (c) show the applied magnetic field and temperature time dependence, respectively. The maximum temperature reached during the protocol ($T = 15$ (K)) was above the highest T_c reported for this material in the literature. As seen in the reduced magnetic moment's response to the applied field, the moment initially exhibits a non-linear increase with field intensity, growing for fields lower than $H = 0.19$ (T). At higher fields, the growth rate increases further and shows no sign of saturation up to about $H = 0.2$ (T), beyond this point, the rate of change in the magnetic moment decreases and gradually approaches saturation for fields up to 0.5 (T).

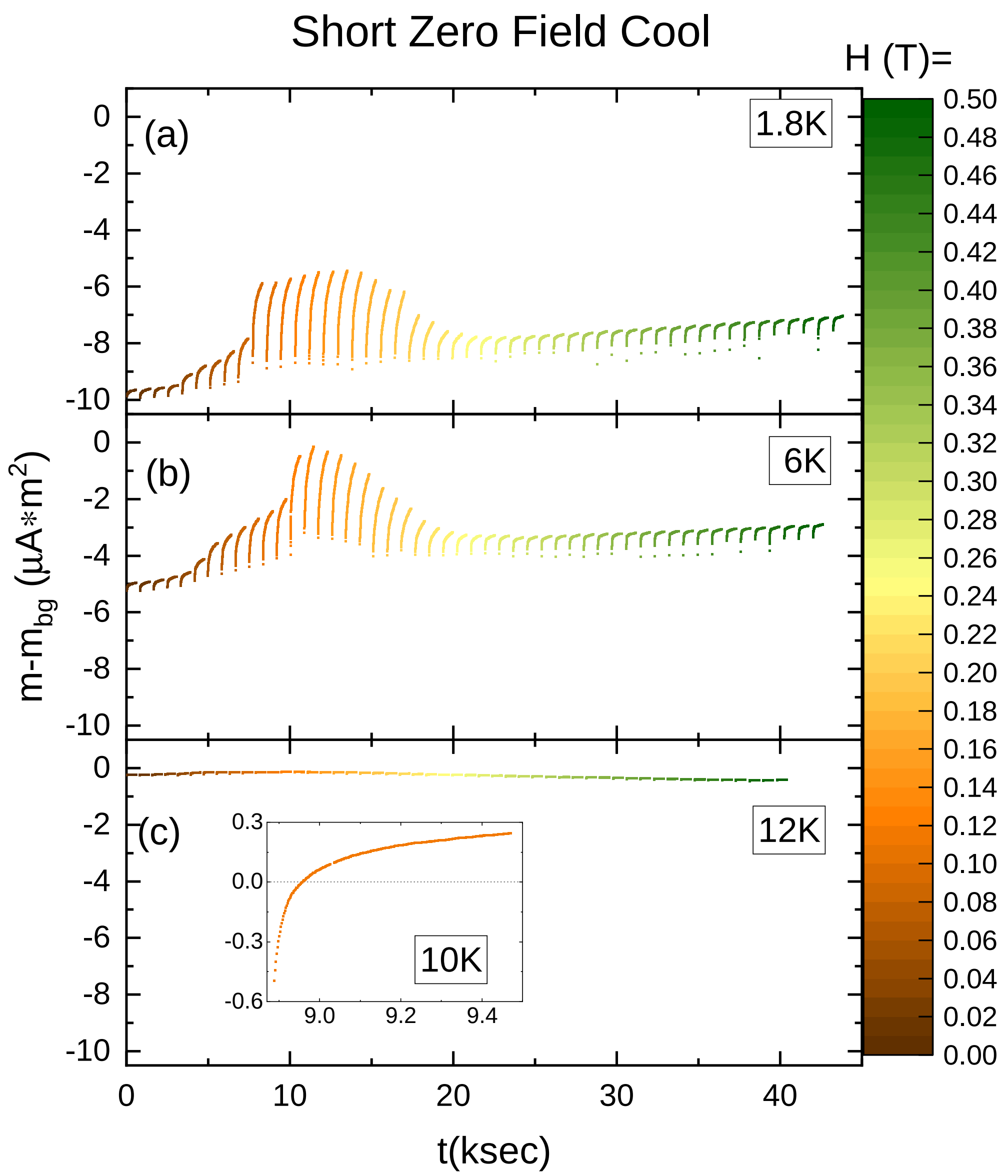

Figure 5.8: Panels (a), (b), (c) shows the time dependence of the background subtracted magnetic moment under the ZFC protocol at $T = 1.8,\ 6,\ 12\ (K)$ base temperatures respectively. The color of each curve indicates the applied magnetic field. The inset in panel (c) which corresponds to $T = 10\ (K)$ and $H = 0.12\ (T)$, highlights that the measured moment can switch between positive and negative values. As temperature increases, the initial moment at $t = 0\ (sec)$ shifts toward zero and the saturation time shortens.

In order to investigate the temperature dependence under the ZFC protocol (outlined in Table 3.1), we performed measurements at several base temperatures. The results are shown in Figure 5.8, where the color of each curve corresponds to the applied field. In all cases the LAO background was subtracted from the signal. As the temperature increases (panels (b) and (c), $T = 6$ and 12 K, respectively), the initial moment at $t = 0$ s approaches zero compared to panel (a) which corresponds to $T = 1.8$ (K), and the characteristic saturation time of the curves shortens. For all temperatures and applied fields we observe a non-linear magnetic response as a function of time, exhibiting a recurring structure of short saturation times, followed by long saturation times, and then short times again as a function of applied field. The inset in panel (c) which corresponds to $T = 10$ (K) and $H = 0.12$ (T) demonstrates that the measured moment can switch between positive and negative values.

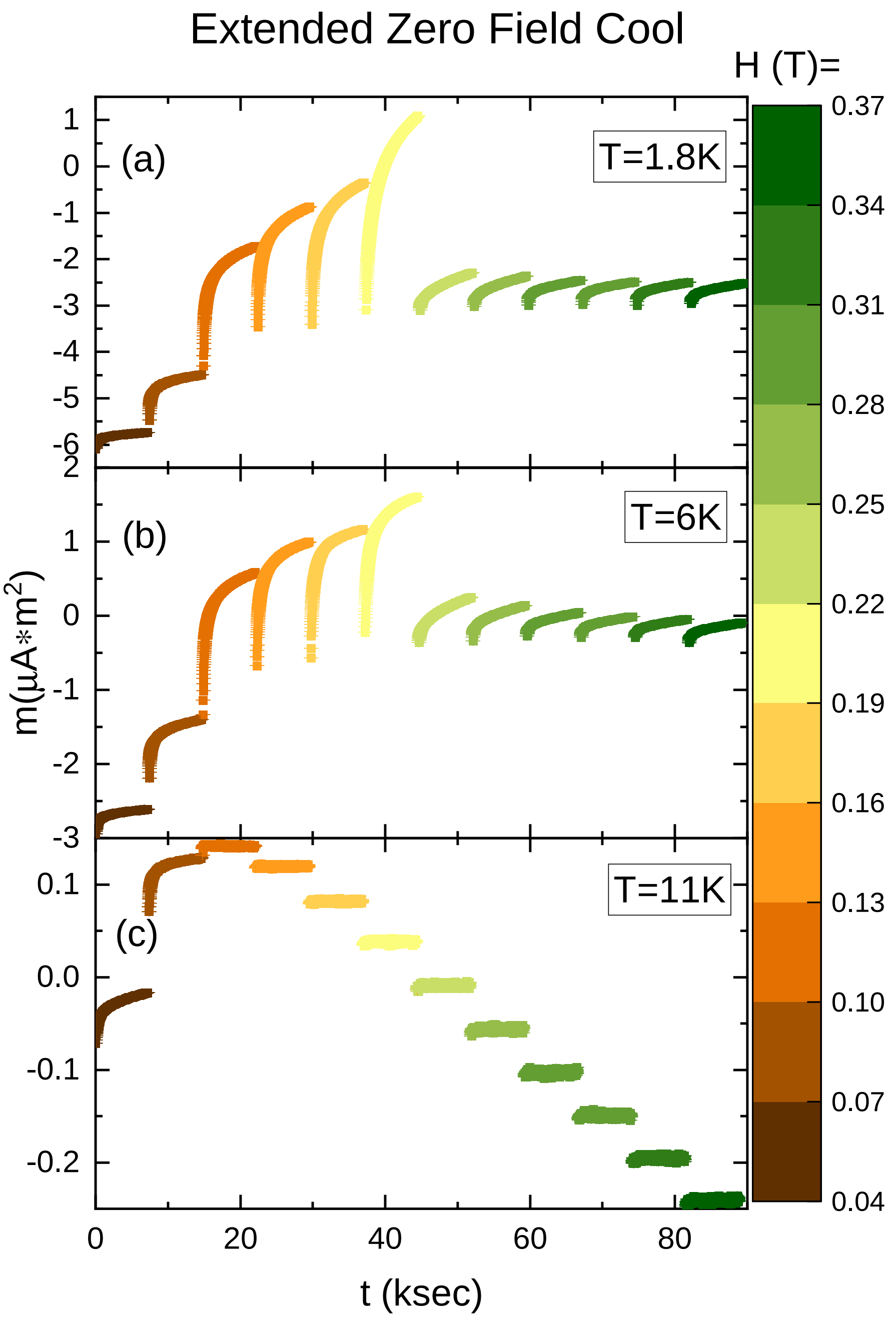

Figure 5.9: Time dependence of the magnetic moment under the ZFC protocol for extended measurement times ($\Delta t = 7.2$ $(ksec)$). While most fields and temperatures in panels (a) and (b) the correspond to $T = 1.8,\ 6$ (K) respectively, exhibit saturation over the extended interval, the response near $H = 0.19$ (T) at low temperatures does not fully saturate. Close to the critical temperature, as seen in panel (c) which corresponds to $T = 11$ (K), the response becomes comparable to that of the film (see Figure 5.1), indicating that measurements slightly above T_c enable separation of the superconducting contribution from the substrate background.

For the measured time interval of $\Delta t = 0.6$ $(ksec)$ some magnetic moments do not appear to reach saturation and can only be distinguished by their initial response, as shown in Figure 5.8. To investigate the long-time behavior, we extended the measurement window to $\Delta t = 7.2$ $(ksec)$ as presented in Figure 5.9. Over this extended interval, the magnetic response at most fields and temperatures saturates as seen in panels (a) and (b) that represent the base temperatures $T = 1.8$ (K) and $T = 6$ (K) respectively, however, at $H = 0.19$ (T) and in panel (a), the response does not fully saturate. Additionally, near the critical temperature as seen in panel (c) which corresponds to $T = 11$ (K), the response is comparable in magnitude to that of the film, as seen in Figure 5.1, (noting that the maximum applied field is approximately twice that in the inset, and the temperatures correspond to the peak response). From this, we infer that measurements slightly above the critical temperature, may allow us to isolate the superconducting contribution by subtracting the sample's response above the critical temperature.

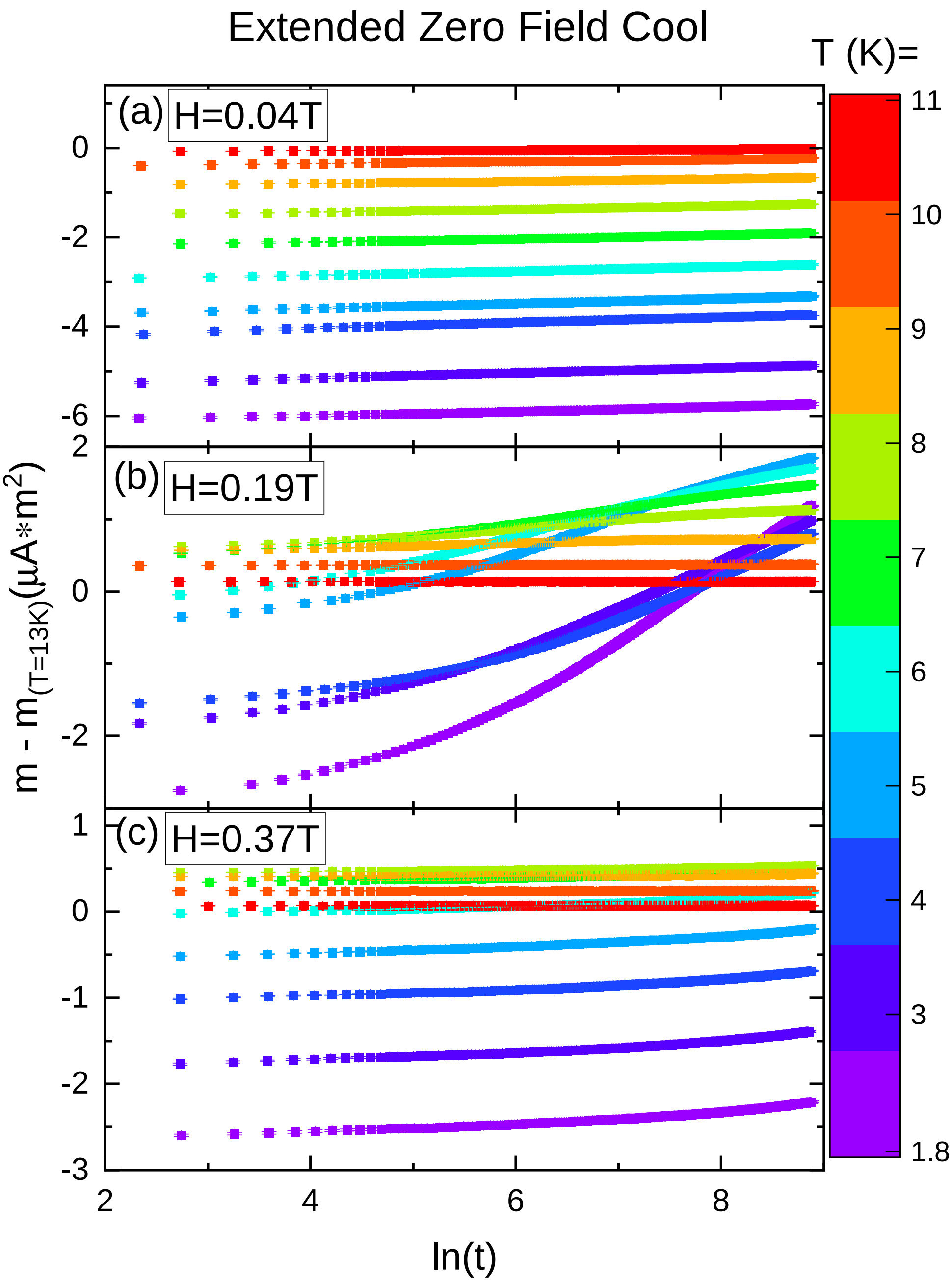

Figure 5.10: Superconducting moment as a function of the natural logarithm of time under the ZFC protocol for three representative fields: $H = 0.04,\ 0.19,\ 0.37\ (T)$ in panels (a), (b) and (c) respectively, across all measured temperatures. For low and high fields the response is approximately linear, while at $H = 0.19\ (T)$ (panel (b)) it becomes strongly nonlinear. At low fields (panel (a)) the response magnitude follows the expected temperature dependence, whereas at higher fields (panel (c)) and for $T > 7\ (K)$ a slight reduction in the response magnitude is observed.

In Figure 5.10, the superconducting moment is plotted as a function of the natural logarithm of time for three representative fields: $H = 0.04,\ 0.19,\ 0.37\ (T)$ in panels (a), (b) and (c) respectively across all measured temperatures. For both low (panel (a)) and high (panel (c)) applied fields, the response appears approximately linear over the entire temperature range, whereas at $H = 0.19\ (T)$ (panel (b)) the response is strongly non-linear. Furthermore, at low applied fields (panel (a)) the magnitude of the response follows the expected temperature dependence, while at higher fields (panel (c)) for temperatures above $T = 7\ (K)$ a slight reduction in the response magnitude is observed.

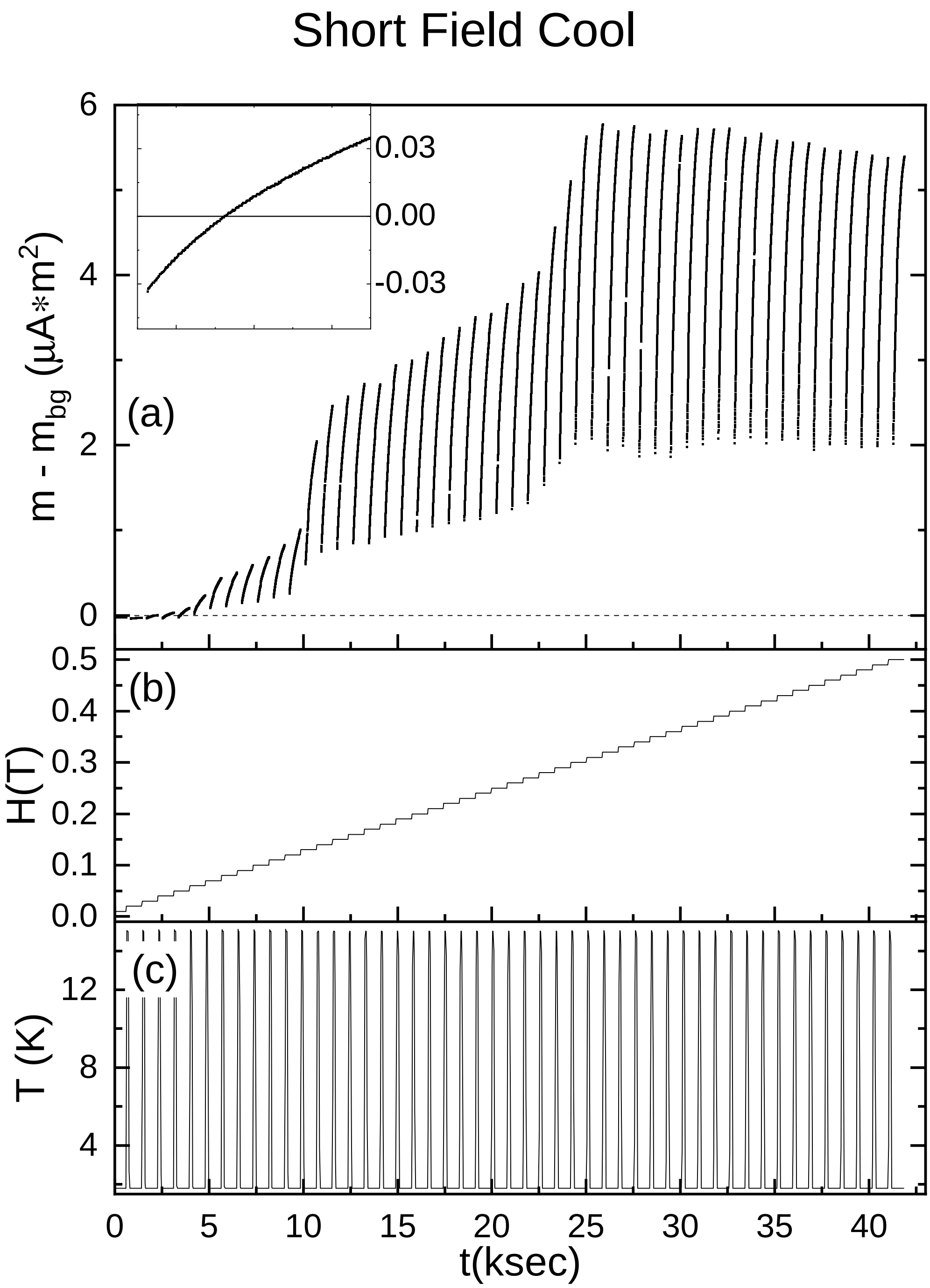

Figure 5.11: Panel (a) shows the subtracted magnetic moment of the $Fe_ySe_xTe_{1-x}$ film as a function of time under the field-cool (FC) protocol at $T = 1.8$ (K). The response shows non-linear growth with increasing field, with distinct changes in slope around $H = 0.05,\ 0.15,\ 0.25$ (T), while no additional regimes are observed at higher fields. The inset in panel (a) demonstrates the switch between negative and positive moments. Panels (b) and (c) show the field and temperature time dependence respectively.

Figure 5.11(a) shows the subtracted magnetic moment (i.e. the measured moment of the $Fe_ySe_xTe_{1-x}$ film with the substrate minus the substrate's magnetic response) as a function of time alongside the applied magnetic field and temperature, for a constant base temperature $T = 1.8$ (K) under the field-cool (FC) protocol. The maximum temperature reached during this protocol ($T = 15$ (K)) exceeds the highest reported T_c for this material in the literature. As seen in the reduced magnetic moment, the response initially exhibits a non-linear increase with field intensity, growing steadily for $H < 0.05$ (T). At higher fields, the growth rate increases further, showing no sign of saturation up to about $H \approx 0.15$ (T). Beyond this point, the rate of change in the magnetic moment increases again until $H \approx 0.25$ (T), where another sharp rise is observed. For higher applied fields, no additional regimes are identified within the measured range. The inset in panel (a) demonstrates the switch between negative and positive moments. Panels (b) and (c) show the field and temperature time dependence respectively.

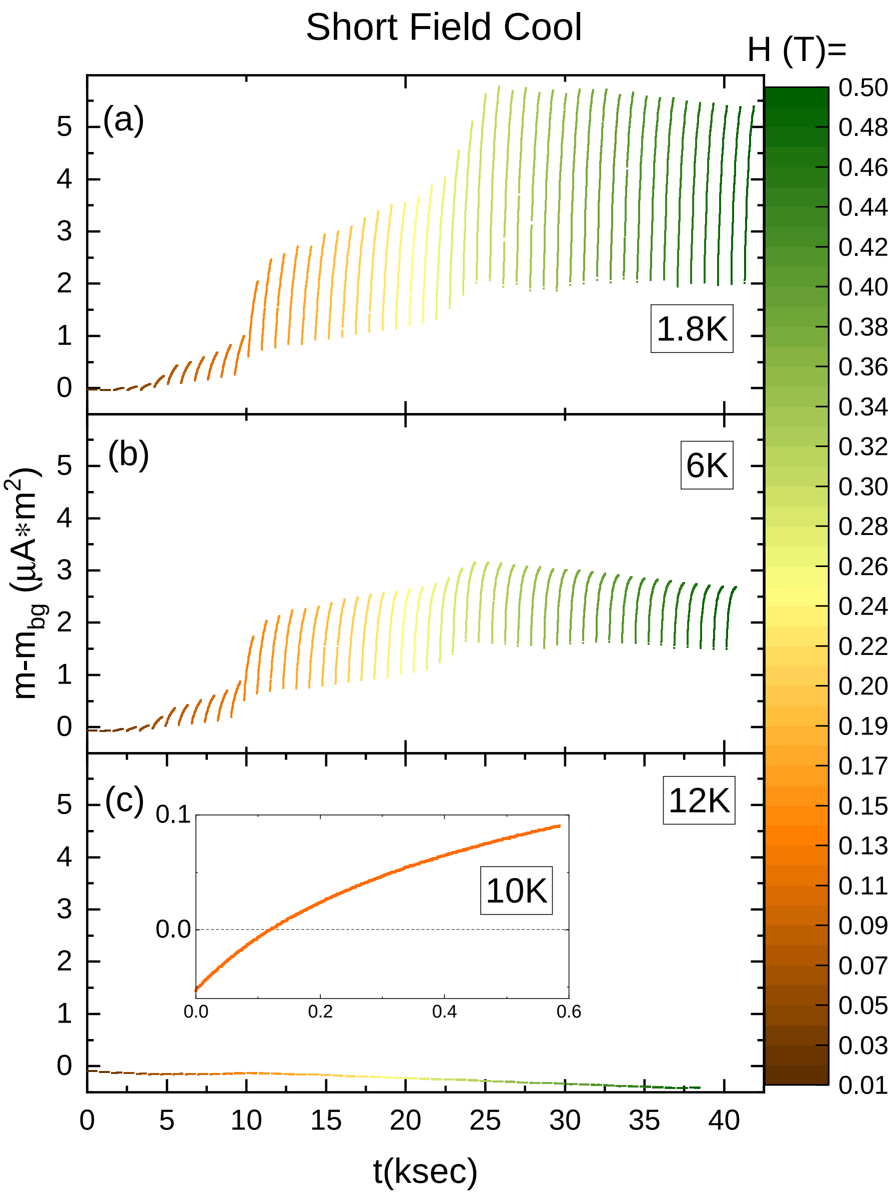

Figure 5.12: Time dependence of the magnetic moment under the FC protocol at several base temperatures: $T = 1.8,\ 6,\ 12\ (K)$, in panels (a), (b) and (c) respectively with curves colored by the applied field. The LAO background has been subtracted from all measurements. The data show a predominantly positive response. With increasing temperature (panels (b) and (c) and inset in (c)), both the initial moment and the overall change in moment decrease toward zero, and no clear saturation is observed. As seen in panel (a) the non-linear time dependence follows the same four-regime structure as in Figure 5.11, with the high-field regime suppressed first (panel (b) and (c)). The inset in panel (c) showing the response for $T = 10\ (K)$ and $H = 0.06\ (T)$ highlights instances where the measured moment switches between positive and negative values.

In order to investigate the temperature dependence under the FC protocol (outlined in Table 3.2), we performed measurements at several base temperatures: $T = 1.8,\ 6,\ 12\ (K)$, in panels (a),(b) and (c) respectively. The results are presented in Figure 5.12, where the color of each curve represents the applied field. In all cases, the LAO background was subtracted from the measured signal. We note that for nearly all measured combinations of field and temperature, the measured moments remain positive, indicating that the total response of the sample is aligned with the applied field. As the temperature increases (panels (b) and (c) and inset in (c)), both the initial moment at time $t = 0$ (sec) and the overall change in moment approach zero, and no clear saturation can be discerned. For all temperatures and applied fields, the magnetic response exhibits a non-linear time dependence, displaying the same four regimes observed in Figure 5.11, with the high-field regime being suppressed first. The inset in panel (c) showing the response for $T = 10$ (K) and $H = 0.06$ (T) further illustrates that the measured moment can switch between positive and negative values.

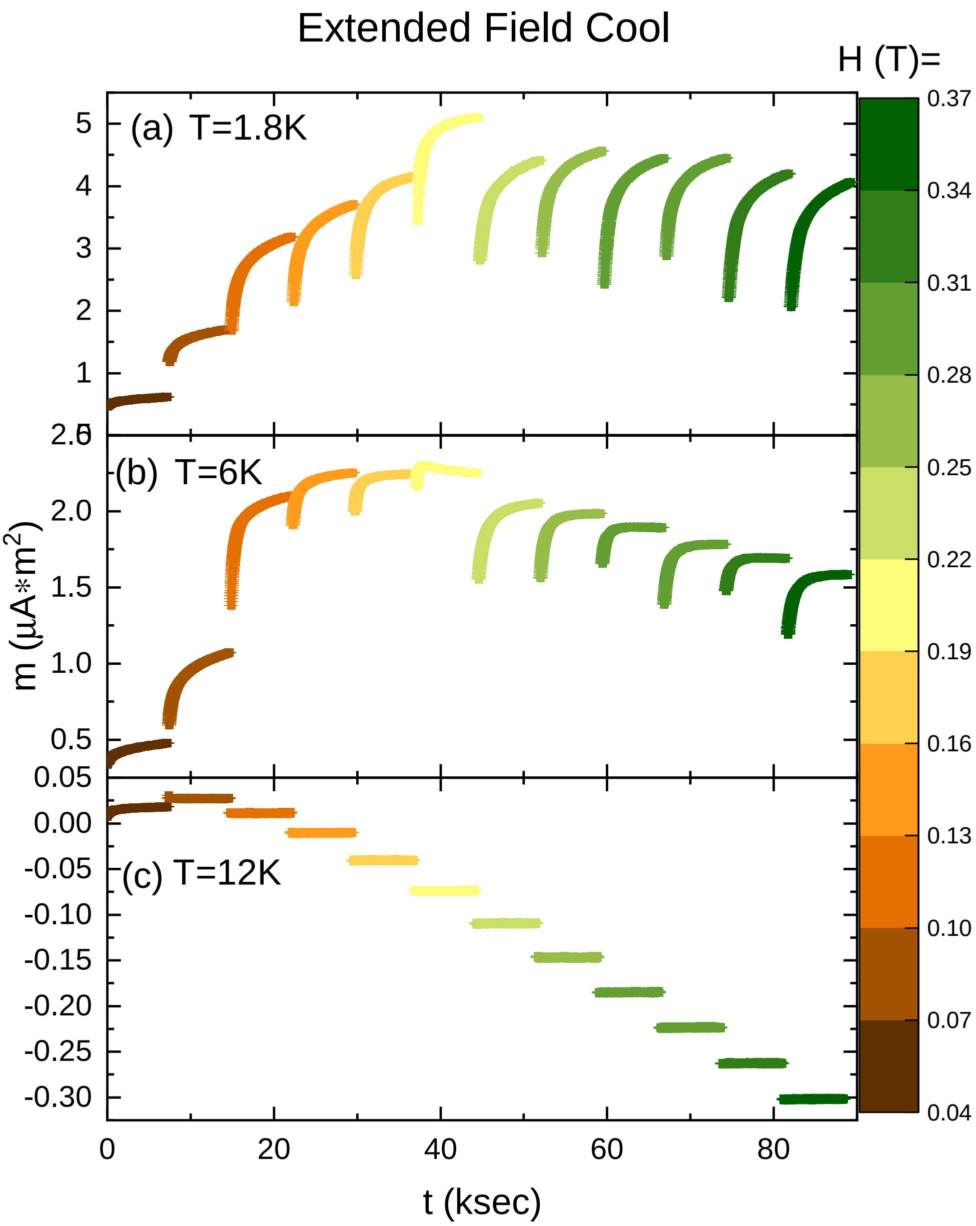

Figure 5.13: Magnetic moment as a function of time under the FC protocol for $T = 1.8$ (K) panel (a), $T = 6$ (K) panel (b), and $T = 12$ (K) panel (c), for measurement window $\Delta t = 7.2$ $(ksec)$ reveals saturation at higher temperatures (panels (b) and (c)), while at low temperatures (panel (a)) the response remains unsaturated. Near T_c (panel (c)), the magnitude of the response approaches that of the film itself (see Figure 5.1), suggesting that measurements slightly above T_c may allow the superconducting contribution to be isolated. The differences observed between FC and ZFC protocols [compare Figure 5.13(c) and Figure 5.9(c)] are attributed to trapped flux in the superconducting state.

For the short measurement interval ($\Delta t = 0.6$ $(ksec)$) most magnetic moments do not appear to saturate and can be distinguished by their initial response and the overall change, as shown in Figure 5.12. To investigate the long-time behavior, we extended the measurement window to $\Delta t = 7.2$ $(ksec)$ at the expense of the number of fields investigated as presented in Figure 5.13. Over this extended interval, the magnetic response saturates for most fields at higher temperatures as seen in panels (b) and (c) which correspond to $T = 6$ (K) and $T = 12$ (K) respectively, however, at lower temperatures, as seen in Figure 5.13(a) which corresponds to $T = 1.8$ (K), the response does not fully saturate for the majority of fields. Additionally, near the critical temperature (panel (c)), the response is comparable in magnitude to that of the film itself, as seen in Figure 5.1, where the maximum applied field is approximately twice the intensity and the temperature corresponds to that of the peak response in the inset. From this we infer that measurements slightly above the critical temperature may allow the superconducting contribution to be isolated by subtracting the sample's response above the critical temperature. Finally, we note the apparent difference between Figure 5.13(c) and Figure 5.9(c), which we attribute to the distinct response of the superconducting state under the two protocols, specifically the trapped flux within the sample.

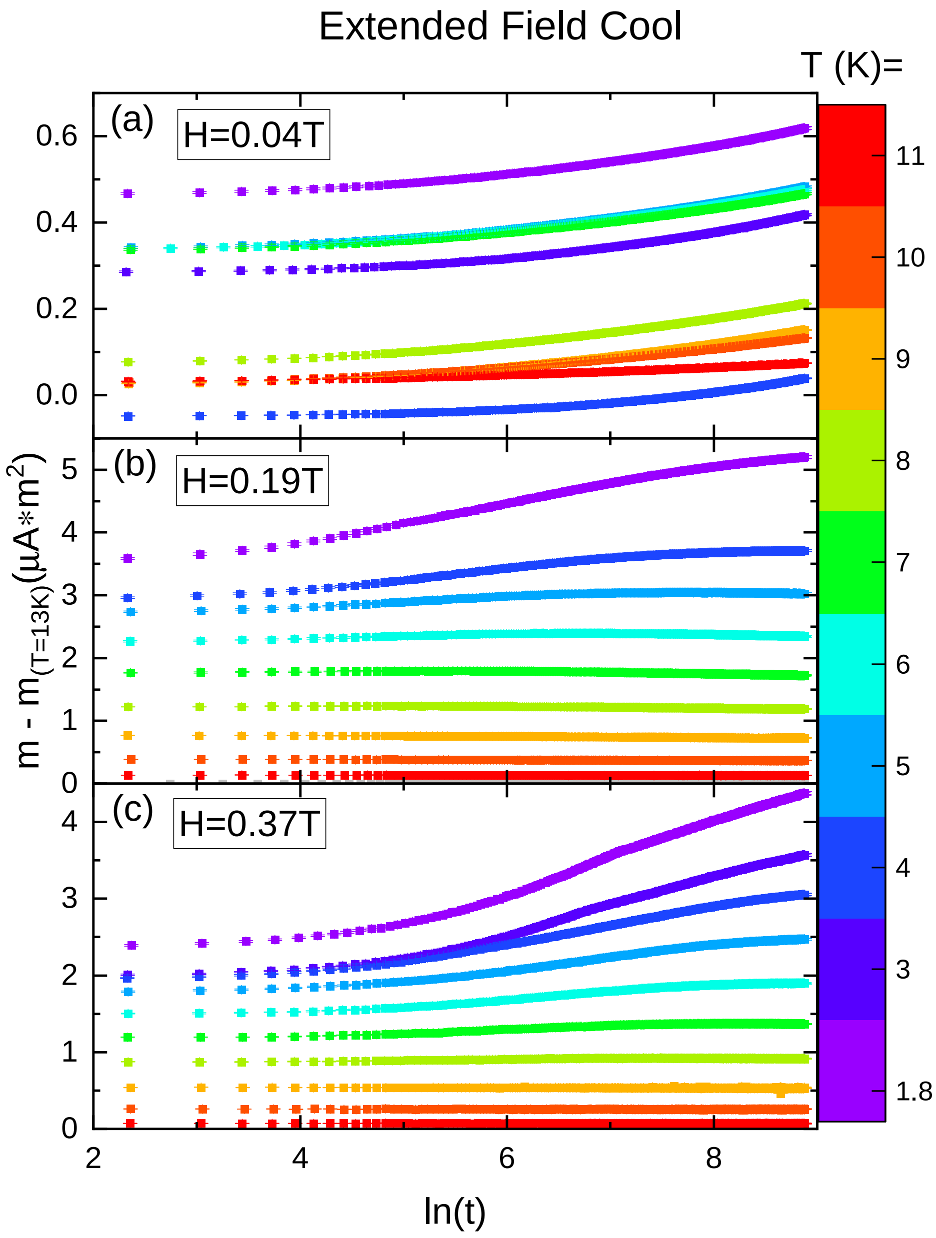

Figure 5.14: Superconducting moment plotted as a function of the natural logarithm of time under FC protocol for three representative applied fields: $H = 0.04,\ 0.19,\ 0.37\ (T)$ which corresponds to panels (a), (b) and (c), across all measured temperatures. The response is predominantly non-linear, except near the critical temperature (seen in red in all panels). At low fields (panel (a)), the magnitude of the response deviates from the expected temperature dependence, while at higher fields (panels (b) and (c)) the expected behavior is recovered.

In Figure 5.14, the superconducting moment is plotted as a function of the natural logarithm of time for the same three representative fields: $H = 0.04,\ 0.19,\ 0.37\ (T)$ which corresponds to panels (a), (b) and (c) in Figure 5.10, across all measured temperatures. For all applied fields, the response remains largely non-linear over the entire temperature range, except in the vicinity of the critical temperature (seen in red in all panels). At low applied fields, as shown in panel (a), the magnitude of the response deviates from the expected temperature dependence, whereas at higher fields, shown in panels (b) and (c) response exhibits the expected temperature dependence.

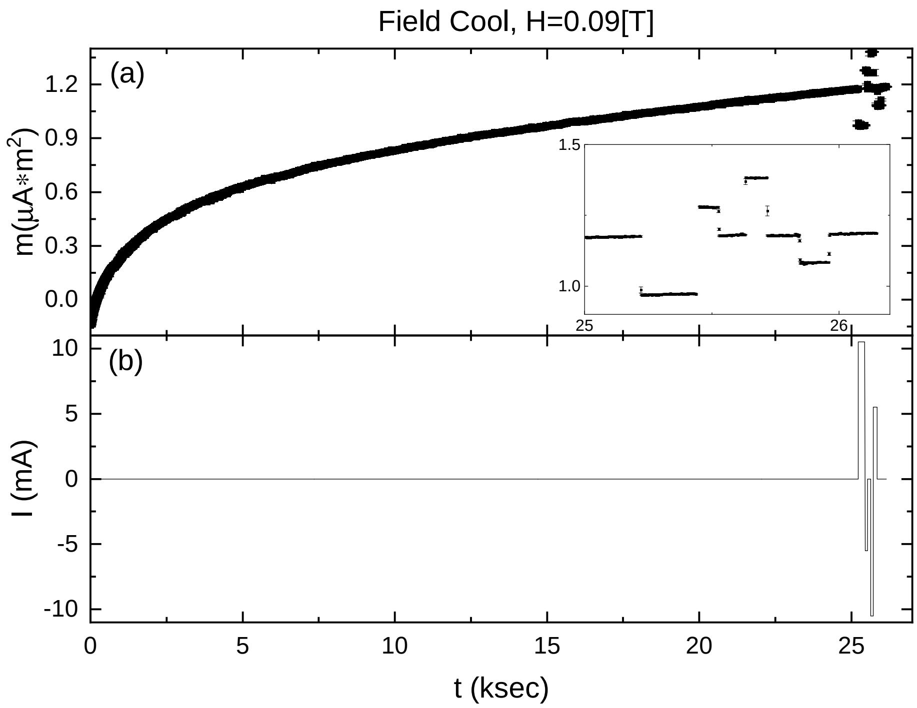

Figure 5.15: Field-cooled measurement at $T = 1.8\ (K)$ and $H = 0.09\ (T)$ over an extended time interval. Panel (b) shows the modulation of the excitation coil current, while panel (a) and the inset present the superconducting response. The magnetic moment switches sign. Upon applying a vector potential, the observed signal remains both persistent and proportional to the applied vector potential.

To determine whether the measured response originates from a superconducting contribution or from another magnetic source, we performed a FC protocol at a base temperature of $T = 1.8\ (K)$ and applied field of $H = 0.09\ (T)$ with the excitation coil current I=0(A), over an extended time period. During this measurement, the magnetic moment switched from negative to positive. The first measurement window lasted approximately $\Delta t = 25\ (ksec)$ and was followed by a second window during which the excitation coil current was modulated, as shown in panel (b). The corresponding superconducting response is presented in panel (a) and in the inset, where the magnitude of the signal is clearly both persistent and proportional to the modulating vector potential. The same modulation was performed under ZFC protocol, yielding similar results.

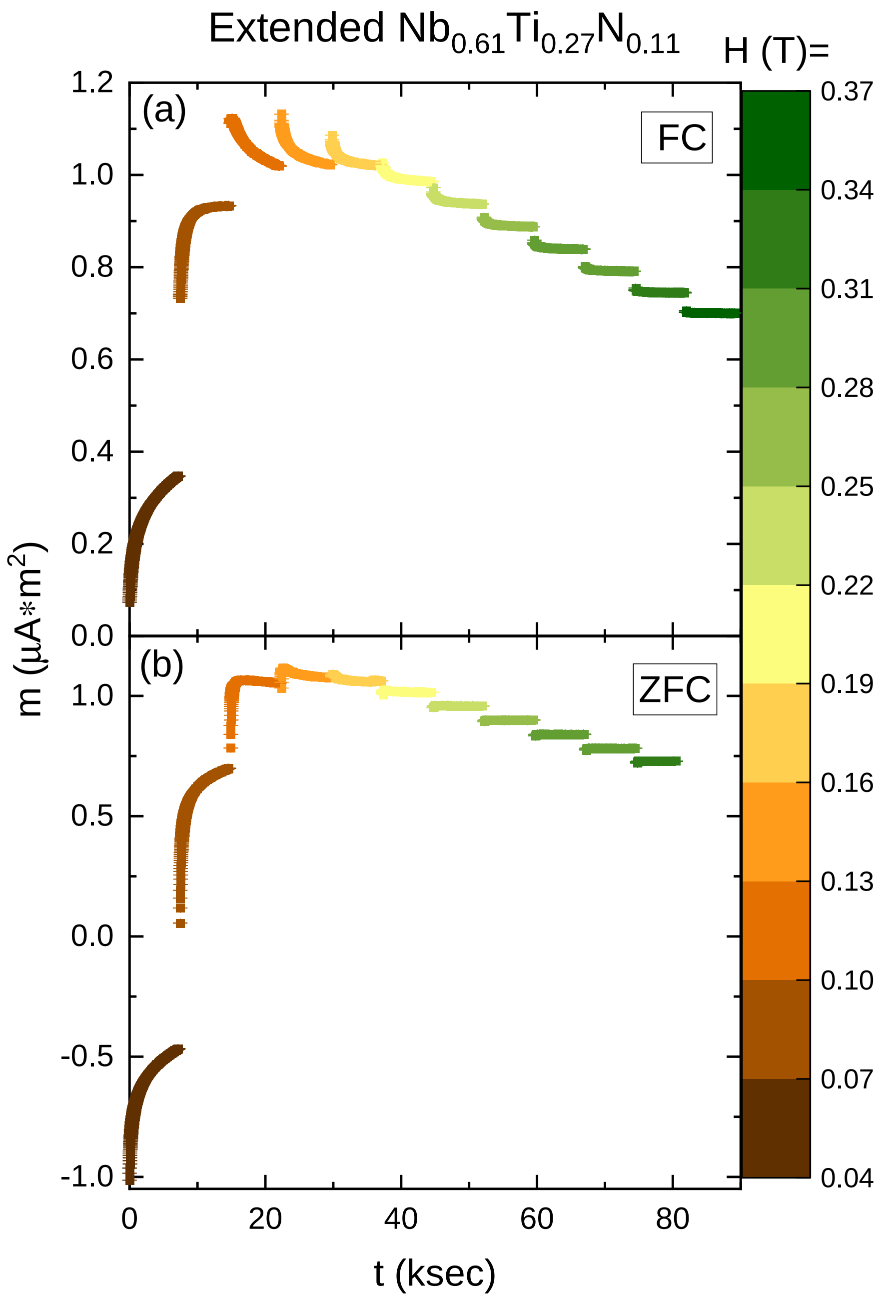

Figure 5.16: Magnetic moment as a function of time for a $Nb_{0.61}Ti_{0.27}N_{0.11}$ ring with geometry comparable to the $Fe_ySe_xTe_{1-x}$ samples, measured under extended time windows for (a) FC and (b) ZFC protocols. In both cases a clear time-dependent response is observed: (a) a positive response decreasing toward saturation for fields above $H = 0.1$ (T), and (b) a response that interpolates between negative and positive values, with a notable decrease in moment around $H = 0.13T$. The comparison with $Fe_ySe_xTe_{1-x}$ indicates that the time dependence originates from a geometric effect of the superconducting ring.

To isolate the origin of the time dependence, we performed extended measurements ($\Delta t = 7.2$ ($ksec$) under both FC and ZFC on a $Nb_{0.61}Ti_{0.27}N_{0.11}$ ring with comparable annular dimensions and thickness (Figure 5.16, panels (a) and (b)). In panel (a), we observe a positive response with clear time dependence, while in panel (b) we again see a time-dependent response, which can be interpreted as switching between negative and positive values. Notably, unlike the response observed in Figure 5.13, the response in Figure 5.16(a) for applied fields higher $H = 0.1$ (T), decreases toward zero and saturates rather than increasing. Similarly, the response shown in Figure 5.9 differs from that in Figure 5.16(b), where for applied fields above $H = 0.1$ (T) the moment decreases, most prominently around $H = 0.13$ (T). From these comparisons, we conclude that the observed time dependence is a geometric effect of the superconducting ring.

Chapter 6

Conclusions

Magnetic Order: In Figure 5.1 we showed that the $Fe_ySe_{0.5}Te_{0.5}$ film (d=80[nm]) exhibits a weak magnetic response on the order of $m = 0.1\mu A \cdot m^2$ which does not conform to conventional paramagnetic or ferromagnetic behavior.

Stiffnessometer: In Figure 5.2 we reproduced the ”knee” observed by Peri et al [5], and in Figure 5.3 (b) demonstrated that it most likely corresponds to the opening of a second superconducting gap, as revealed by the comparison of the normalized stiffness (blue) to the BCS theoretical curve (red).
These results are in partial agreement with [22] where the larger gap that corresponds to the onset of superconductivity is approximately 80% larger than the value measured in our experiment. We further note deviations from the conventional BCS model as seen in Figure 5.3, particularly near the onset of superconductivity, where the stiffness exhibits an unusually rapid increase compared to the expected behavior of standard s-wave pairing. We propose a possible explanation where the onset of superconductivity occurs at a temperature roughly 1K higher than the value observed in our measurements, but the threshold for a measurable moment requires a more substantial supercurrent, causing the apparent discrepancy between the slope of the expected BCS curve and that of our measurements, as seen in Figure 5.3 (b) in the blue and red curves, respectively. Another possible explanation is the presence of an unconventional pairing mechanism that isn't described by standard BCS theory. We finally note that the opening of the gaps was not observed in the ξ measurements, as shown in Figure 5.3(a) (green), in contrast to the clear ”knee” seen in the inverse pearl length (blue).

Geometric Effect: In Figures 5.7 - 5.14 we showed that both ZFC and FC protocols produce time-dependant magnetization. We attribute this behavior to flux dynamics in thin films based on two observations: first, as seen in Figure 5.15 the magnetization responds to modulations of the vector potential, indicating that the effect is associated with the superconducting condensate. Second, similar time-dependence arises in other samples of comparable geometry such as $Nb_{0.61}Ti_{0.27}N_{0.11}$ as seen in Figure 5.16. This is in contrast to measurements performed on bulk samples on the same material by Peri et. al that showed no time dependence [5]. These time-dependent responses can switch between negative and positive values in both ZFC and FC protocols. Extended ZFC measurement reveal saturation for most temperatures and fields, except for fields close to $H = 0.19(T)$ as seen in Figure 5.9.

The superconducting contribution to the moment under the ZFC conditions behaves roughly linearly with the natural logarithm of time, $ln(t)$, for most fields and temperatures, but shows strong nonlinearity at certain fields as seen in Figure 5.10. Furthermore, while the response magnitude follows the expected temperature dependence at low fields, it decreases at higher fields for temperatures above T=7(K) as seen in Figures 5.8 and 5.9 and most clearly in Figure 5.10.

In contrast, under FC conditions, the superconducting contribution to the moment in the FC protocol is approximately linear in $ln(t)$ only at small fields and high temperatures, but strongly nonlinear for most other fields as seen in Figure 5.14. Here, the magnitude of the response follows the expected temperature dependence at medium and high fields, whereas at low applied fields it increases for temperatures above T=6(K). Near T_c, the response becomes comparable in magnitude to the film's intrinsic magnetic signal.

We propose that the differences between ZFC and FC arise from distinct flux dynamics: in ZFC, flux penetrates the sample in it's superconducting state, while in FC, flux exits the sample as it is cooled in the applied field. We note that, due to the temporal character of the magnetization, standard methods to characterize the pinning regime in our sample, such as the Dew-Hughes approach [14] and the established framework of collective flux creep [12] are incompatible with our data.

Bibliography

[1] Michael Tinkham. *Introduction to Superconductivity, 2nd Edition.* McGraw-Hill, 1996.

[2] Takasada Shibauchi, Tetsuo Hanaguri, and Yuji Matsuda. Exotic superconducting states in fese-based materials. *Journal of the Physical Society of Japan*, 89(10):102002, 2020.

[3] Y. Lubashevsky, E. Lahoud, K. Chashka, et al. Shallow pockets and very strong coupling superconductivity in fese$_x$te$_{1x}$. *Nature Physics*, 8:309–312, 2012.

[4] Himanshu Lohani, Tamaghna Hazra, Amit Ribak, Yuval Nitzav, Huixia Fu, Binghai Yan, Mohit Randeria, and Amit Kanigel. Band inversion and topology of the bulk electronic structure in fese$_{0.45}$te$_{0.55}$. *Phys. Rev. B*, 101:245146, Jun 2020.

[5] Amotz Peri, Itay Mangel, and Amit Keren. Superconducting stiffness and coherence length of fese0.5te0.5 measured in a zero-applied field. *Condensed Matter*, 8(2), 2023.

[6] Amit Keren, Nitsan Blau, Nir Gavish, Oded Kenneth, Yachin Ivry, and Mohammad Suleiman. Stiffness and coherence length measurements of ultra-thin superconductors, and implications for layered superconductors. *Superconductor Science and Technology*, 35(7):075013, jun 2022.

[7] P.-G. De Gennes and P. A. Pincus. *Superconductivity of Metals and Alloys.* CRC Press, Boca Raton, FL, USA, 2018.

[8] A. Carrington and F. Manzano. Magnetic penetration depth of mgb2. *Physica C: Superconductivity*, 385(1):205–214, 2003.

[9] R. Gupta, D. Das, C. H. Mielke III, et al. Microscopic evidence for anisotropic multigap superconductivity in the CsV_3Sb_5 kagome superconductor. *npj Quantum Materials*, 7:49, 2022.

[10] M. Bendele, S. Weyeneth, R. Puzniak, A. Maisuradze, E. Pomjakushina, K. Conder, V. Pomjakushin, H. Luetkens, S. Katrych, A. Wisniewski, R. Khasanov, and H. Keller. Anisotropic superconducting properties of single-crystalline fese$_{0.5}$te$_{0.5}$. *Phys. Rev. B*, 81:224520, Jun 2010.

[11] J. Pearl. Current distribution in superconducting films carrying quantized fluxoids. *Applied Physics Letters*, 5(4):65–66, 08 1964.

[12] M. V. Feigel'man, V. B. Geshkenbein, A. I. Larkin, and V. M. Vinokur. Theory of collective flux creep. *Physical Review Letters*, 63(20):2303–2306, November 1989.

[13] A.A. Abrikosov. The magnetic properties of superconducting alloys. *Journal of Physics and Chemistry of Solids*, 2(3):199–208, 1957.

[14] D. Dew-Hughes. Flux pinning mechanisms in type ii superconductors. *The Philosophical Magazine: A Journal of Theoretical Experimental and Applied Physics*, 30(2):293–305, 1974.

[15] Y. Yeshurun, A. P. Malozemoff, and A. Shaulov. Magnetic relaxation in high-temperature superconductors. *Reviews of Modern Physics*, 68(3):911–949, July 1996.

[16] Charles Kittel. *Introduction to Solid State Physics, 8th Edition.* John Wiley & Sons, Hoboken, NJ, USA, 2005.

[17] K. Mukasa, K. Matsuura, M. Qiu, and et al. High-pressure phase diagrams of fese$_{1x}$te$_x$: correlation between suppressed nematicity and enhanced superconductivity. *Nature Communications*, 12:381, 2021.

[18] Despina Louca, K. Horigane, A. Llobet, R. Arita, S. Ji, N. Katayama, S. Konbu, K. Nakamura, T.-Y. Koo, P. Tong, and K. Yamada. Local atomic structure of superconducting fese$_{1-x}$te$_x$. *Phys. Rev. B*, 81:134524, Apr 2010.

[19] K. Momma and F. Izumi. Vesta 3 for three-dimensional visualization of crystal, volumetric and morphology data. *Journal of Applied Crystallography*, 44:1272–1276, 2011.

[20] Weidong Si, Juan Zhou, Qing Jie, Ivo Dimitrov, V. Solovyov, P. D. Johnson, J. Jaroszynski, V. Matias, C. Sheehan, and Qiang Li. Iron-chalcogenide fese0.5te0.5 coated superconducting tapes for high field applications. *Applied Physics Letters*, 98(26):262509, 07 2011.

[21] Amalia I. Coldea and Matthew D. Watson. The key ingredients of the electronic structure of fese. *Annual Review of Condensed Matter Physics*, 9(Volume 9, 2018):125–146, 2018.

[22] T. E. Kuzmicheva, S. A. Kuzmichev, A. V. Sadakov, et al. Direct evidence of two superconducting gaps in fese$_{0.5}$te$_{0.5}$: Sns-andreev spectroscopy and the lower critical field. *JETP Letters*, 104:852–858, 2016.

[23] M. Roppongi, Y. Cai, K. Ogawa, and et al. Topology meets time-reversal symmetry breaking in fese$_{1x}$te$_x$ superconductors. *Nature Communications*, 16:6573, 2025.

[24] Shiyu Zhu, Lingyuan Kong, Lu Cao, Hui Chen, Michał Papaj, Shixuan Du, Yuqing Xing, Wenyao Liu, Dongfei Wang, Chengmin Shen, Fazhi Yang, John Schneeloch, Ruidan Zhong, Genda Gu, Liang Fu, Yu-Yang Zhang, Hong Ding, and Hong-Jun Gao. Nearly quantized conductance plateau of vortex zero mode in an iron-based superconductor. *Science*, 367(6474):189–192, 2020.

[25] Zhenyu Wang, Jorge Olivares Rodriguez, Lin Jiao, Sean Howard, Martin Graham, G. D. Gu, Taylor L. Hughes, Dirk K. Morr, and Vidya Madhavan. Evidence for dispersing 1d majorana channels in an iron-based superconductor. *Science*, 367(6473):104–108, 2020.

[26] Weidong Si, Juan Zhou, Qing Jie, Ivo Dimitrov, V. Solovyov, P. D. Johnson, J. Jaroszynski, V. Matias, C. Sheehan, and Qiang Li. Iron-chalcogenide fese0.5te0.5 coated superconducting tapes for high field applications. *Applied Physics Letters*, 98(26):262509, 07 2011.

[27] Armando Galluzzi, Krastyo Buchkov, Vihren Tomov, Elena Nazarova, Antonio Leo, Gaia Grimaldi, and Massimiliano Polichetti. High pinning force values of a fe(se, te) single crystal presenting a second magnetization peak phenomenon. *Materials*, 14(18), 2021.

[28] E Bellingeri, S Kawale, V Braccini, R Buzio, A Gerbi, A Martinelli, M Putti, I Pallecchi, G Balestrino, A Tebano, and C Ferdeghini. Tuning of the superconducting properties of fese0.5te0.5 thin films through the substrate effect. *Superconductor Science and Technology*, 25(8):084022, jul 2012.

[29] Itay Mangel, Itzik Kapon, Nitzan Blau, Katrine Golubkov, Nir Gavish, and Amit Keren. Stiffnessometer: A magnetic-field-free superconducting stiffness meter and its application. *Phys. Rev. B*, 102:024502, Jul 2020.

[30] F. Hecht. New development in freefem++. *J. Numer. Math.*, 20(3-4):251–265, 2012.

גיאומטריה דומה (עובי טבעת $d = 80[nm]$). הצלחנו לזהות את מקורה של התלות הזמנית כאפקט גיאומטרי אינהרנטי לטבעות מוליכות-על דקות. השלכות המחקר נוגעות לשני מישורים עיקריים: מישור פיזיקלי-תיאורטי – התוצאות מאתגרות את ההנחה שמודל הצימוד ב $FeSeTe$ הוא מודל הצימוד הסטנדרטי עבור מערכת דו-פערית ומרמזות על מנגנון צימוד אלקטרוני לא שגרתי במערכת זו. מישור ניסויי-מתודולוגי – השימוש בסטיפנסומטר ממחיש כי ניתן לעקוף בעיות מהותיות במדידות מגנטיות במוליכי-על מבוססי ברזל. באופן כללי, עבודתנו מדגישה את החשיבות של מדידות ישירות ומדויקות בקידום ההבנה של מוליכות-על לא קונבנציונלית. לסיכום, המחקר שבוצע: הדגים שימוש אפקטיבי של סטיפנסומטר בחומר $FeSeTe$, חשף עדות לשני פערים על־מוליכים עם תלות טמפרטורה בלתי שגרתית, זיהה את מקור התלות הזמנית של מגנטיזציה כאפקט גיאומטרי בטבעות מוליעות-על דקות. העבודה פותחת פתח למחקרים עתידיים שיבחנו שאלות על מקור הגאומטריה ויבחנו את ההסבר שהוצע במסגרת העבודה הנוכחית כגון יצירת פילם דק בתחום פשוט קשר, וכן שאלות על מנגון הצימוד בחומר $FeSeTe$ בנוגע לסימטריית פונקציית הגל העל-מוליכה. כיצד משתנה התנהגות הקשיחות העל-מוליכה והפערים עבור סימום שונה, ועד כמה ניתן להכליל את הממצאים גם לחומרים אחרים ממשפחת העל־מוליכים מבוססי ברזל?

תקציר

קשיחות העל־מוליך (ρ_s) ואורך הקוהרנטיות (ξ) הם שני פרמטרים מרכזיים בתיאור תכונותיהם הפיזיקליות של מוליכי-על. מקובל לקבוע את ערכם הניסיוני של שני הפרמטרים הללו באמצעות עומק החדירה λ והשדה הקריטי העליון (H_{c2}) בהתאמה. עם זאת, בחומרים על־מוליכים מבוססי ברזל מתעוררת בעיה מהותית: השדה המגנטי השקול בחומר עשוי לסטות באופן ניכר מהשדה המגנטי החיצוני בשל הופעת שדות פנימיים בחומר, וכך מתקבלים ערכים בלתי מדויקים של קשיחות ושל אורך הקוהרנטיות. בעיה זו מקשה על פענוח נכון של מנגנוני מוליכות-על בחומרים אלה, הנחשבים למועמדים מבטיחים להבנה של פיזיקה של מצבים אלקטרוניים קורלטיביים. במחקר זה התמקדנו בטבעות דקות ($d = 80[nm]$) עשויות $\mathrm{Fe}_{1+y}\mathrm{Se}_x\mathrm{Te}_{1-x}$ בהרכב $x = 0.5, y \approx 0$, מבין משפחת החומרים מבוססי הברזל, המבנה הגבישי הפשוט ביותר הוא של FeSe (מבנה PbO טטרגונלי), ועל ידי החלפה של סלניום בטלוריום חלים שינויים קלים במבנה הקריסטלוגרפי אשר מחד מאפשרים תיאור תיאורטי טוב של מבנה הפסים של החומר, ומאידך בשל אפקטי צימוד ספין מסילה והשינויים במבנה הפסים של החומר, נוצרים מצבים אלקטרוניים קורלטיביים וטופולוגיה לא טריוואלית. חלק מהטענות התיאורטיות בחומר זה אומתו באופן ניסיונים בשיטות שונות, לדוגמא: באמצעות ARPES אוששה הטענה להיפוך פסים, ובאמצעות STM נצפו מצבי Zero-Bias בליבות וורטקסים. מדידות שנעשו באמצעות μSR העלו עדויות אפשריות לTRSB. כדי להתגבר על הקשיים הנובעים מהשדות הפנימיים בחומר, השתמשנו בשיטת הסטיפנסומטר. בשיטה זו מפעילים פוטנציאל וקטורי מגנטי (A) חסר רוטור על טבעת מוליכת-על, ומודדים את המומנט המגנטי (m) אשר מתפתח בה. מתוך המדידה ניתן לחלץ את צפיפות הזרם , (j), וכך, באמצעות משוואת לונדון $j = -\rho_s A$, ניתן לקבוע באופן ישיר גם את הקשיחות העל־מוליכה ρ_s וגם את אורך הקוהרנטיות ξ. יתרונו המרכזי של הסטיפנסופמטר הוא יכולתו למדוד גדלים אלה מבלי להסתמך על שדות חיצוניים, ובכך להימנע מהשפעת השדות הפנימיים אשר עשויים להווצר בחומרים מבוססי ברזל. בהשוואה לשיטות המסורתיות, המסתמכות על מדידות של חדירת שטף לחומר או על קביעת השדה הקריטי העליון, H_{c2}, מדובר ביתרון מהותי שמאפשר מדידה ישירה ובלתי מתווכת של פרמטרי גינזבורג-לנאדו התרמודינמיים של החומר. המדידות שביצענו חשפו עדות ברורה לקיומם של שני פערים על-מוליכים בלתי-תלויים. התלות בטמפרטורה של שני הפערים שונה מהמודל המקובל של על־מוליכות קונבנציונאלית המתאורת באמצעות מודל BCS עם מנגנון צימוד מסוג s-wave (צימוד ספינים הפוכי ספין ותנע). ממצא זה מצטרף לעדויות לכך שמוליכי על מבוססי ברזל אינם ניתנים לתיאור פשוט במסגרת התיאוריות הקונבנציונאלית של מוליכות-על, אלא מחייבים התייחסות הן לקורלציות אלקטרוניות חזקות ומעלות את האפשרות למנגנוני צימוד לא סטנדרטיים (כמו סימטריה לא טריוואלית של פונקציית הגל). בנוסף למדידות הקשיחות, יישמנו גם מדידות מגנטיזציה סטנדרטיות תחת שדה חיצוני. באמצעות מדידות אלו חקרנו את התנהגות המגנטיזציה כתלות בזמן, הן בדגימות $FeSeTe$ והן בדגימות של $NbSnN$ בעלות

המחקר נעשה בפקולטה לפיזיקה בהנחיית פרופסור קרן עמית. מחבר חיבור זה מצהיר כי המחקר, כולל איסוף הנתונים, עיבודם והצגתם, התייחסות והשוואה למחקרים קודמים וכו', נעשה כולו בצורה ישרה, כמצופה ממחקר מדעי המבוצע לפי אמות המידה האתיות של העולם האקדמי. כמו כן, הדיווח על המחקר ותוצאותיו בחיבור זה נעשה בצורה ישרה ומלאה, לפי אותן אמות מידה.

הכרת תודה מסורה לטכניון על מימון מחקר זה.

מדידות תלויות זמן של מגנטיזציה וקשיחות בטבעות מוליכות-על דקות

חיבור על מחקר

לשם מילוי חלקי של הדרישות לקבלת התואר
מגיסטר למדעים בפיזיקה

מתן בורנובסקי

הוגש לסנט הטכניון — מכון טכנולוגי לישראל
טבת התשפ"ו חיפה דצמבר 2025

מדידות תלויות זמן של מגנטיזציה וקשיחות בטבעות מוליכות-על דקות

מתן בורנובסקי